Applied Geochemistry 159 (2023) 105839

Contents lists available at ScienceDirect

Applied Geochemistry

journal homepage: www.elsevier.com/locate/apgeochem

Swiss deep drilling campaign 2019–2022: Geological overview and rock properties with focus on porosity and pore-space architecture

M. Mazurek [a,*], T. Gimmi [a,b], C. Zwahlen [a], L. Aschwanden [a], E.C. Gaucher [a], M. Kiczka [a], D. Rufer [a], P. Wersin [a], M. Marques Fernandes [b], M.A. Glaus [b], L.R. Van Loon [b], D. Traber [c], M. Schnellmann [c], T. Vietor [c]

[a] Rock-Water Interaction, Institute of Geological Sciences, University of Bern, Switzerland
[b] Paul Scherrer Institut, Villigen, Switzerland
[c] Nagra, Wettingen, Switzerland

ARTICLE INFO

Editorial handling by Dr. Erika A.C. Neeft

ABSTRACT

A recently completed deep drilling campaign, comprising 9 deep boreholes penetrating the Mesozoic sedimentary sequence of northern Switzerland, yielded >6 km of drillcore. One of the main objectives was to characterise the low-permeability sequence with the lower Jurassic Opalinus Clay in its centre, motivated by the site selection for a deep geological repository for radioactive waste. In this context, the chemical and isotopic composition of the porewater, as well as the mineralogical and petrophysical properties of the rocks, were among the main study targets. In this paper, the main objective was the characterisation of the lithologically diverse Jurassic rock sequence with focus on mineralogy, porosity and pore-space architecture. Given the large amount of data, a well constrained relationship between clay content (relating to fine-grained sheet-silicate minerals) and porosity could be established. Porosity increases with clay content along a concave curve, but in detail minor formation-specific differences of the positions relative to the best-fit curve were identified. These are attributed to the highly variable deposition rates that resulted in different times available for early diagenesis to alter the rock fabric by mineral dissolution and cementation, thereby affecting the compaction behaviour. Pore-size distributions were obtained from N_2 ad-/desorption isotherms. A distinct peak at a radius of 3 nm can be clearly correlated with clay minerals, whereas limestones are dominated by pore sizes in the range of 40–100 nm, and marls show intermediate distributions. A conceptual framework is proposed distinguishing a nanometric porosity that is proportional to the clay content and a contribution of larger pores that are related to the geometric incompatibility between platy clay minerals and isometric calcite or quartz. The contribution of these larger pore is thought to explain the curvature of the clay content-porosity relationship and the more limited compaction of the clay in pressure shadows adjacent to the larger grains. A number of outliers towards high porosity at a given clay content were identified in oolites (most strongly in Fe-rich oolites), sandstones and a unit containing coral-reef material. All these units have in common the presence of competent calcite or quartz grains at the time of deposition, leading to grain-supported fabrics and therefore to a more limited compaction in the interstitial pore space.

* Corresponding author.
E-mail address: martin.mazurek@unibe.ch (M. Mazurek).

https://doi.org/10.1016/j.apgeochem.2023.105839
Received 15 February 2023; Received in revised form 23 June 2023; Accepted 8 November 2023
Available online 24 November 2023

1. Introduction to Special Issue on 'Transport parameters, natural tracer profiles and porewater chemistry derived from the Swiss deep drilling programme in a clay-rich sedimentary sequence'

1.1. Framework

As in many other countries, deep geological disposal is the preferred option to dispose of radioactive waste from industry, research and medicine in Switzerland. In 2008, the Swiss Federal Office of Energy developed a Sectoral Plan that defines the roadmap to identify suited areas and to implement geological repositories for different waste categories (SFOE, 2004). The execution of this science-based process has been (and still is) in the responsibility of Nagra (Swiss National Cooperative for the Disposal of Radioactive Waste), overseen by ENSI (Swiss Federal Nuclear Safety Inspectorate). Stage 1 of the 'Sectoral plan for geological repositories' started from a white map of the country and, based on literature data, applied a series of screening criteria to come up with 6 potentially suited siting regions (Nagra 2008). In Stage 2, considering new 2D seismic data and the results of third-party drillings, the number of potential siting regions was reduced to 3, all considering the Opalinus Clay in northern Switzerland as the potential host rock (BFE 2018). All 3 regions, namely Jura Ost (JO), Nördlich Lägern (NL) and Zürich Nordost (ZNO) are located in the northern part of the country where uplift/erosion rates are small and seismic activity is low (Fig. 1). They constitute the study areas dealt with in this Special Issue.

In the currently ongoing Stage 3, 9 deep boreholes were drilled between March 2019 and April 2022, and simplified profiles are shown in Fig. 2. More detailed profiles including formation names are provided in Fig. S1 of the Supplementary materials. With the exception of Rheinau 1-1, all drillings were vertical. High-quality drillcores were obtained for the section Malm–Muschelkalk (or deeper), yielding in total 6326 m of core with 95 mm diameter. The drilling programme was accompanied by extensive borehole logging, hydraulic testing and groundwater

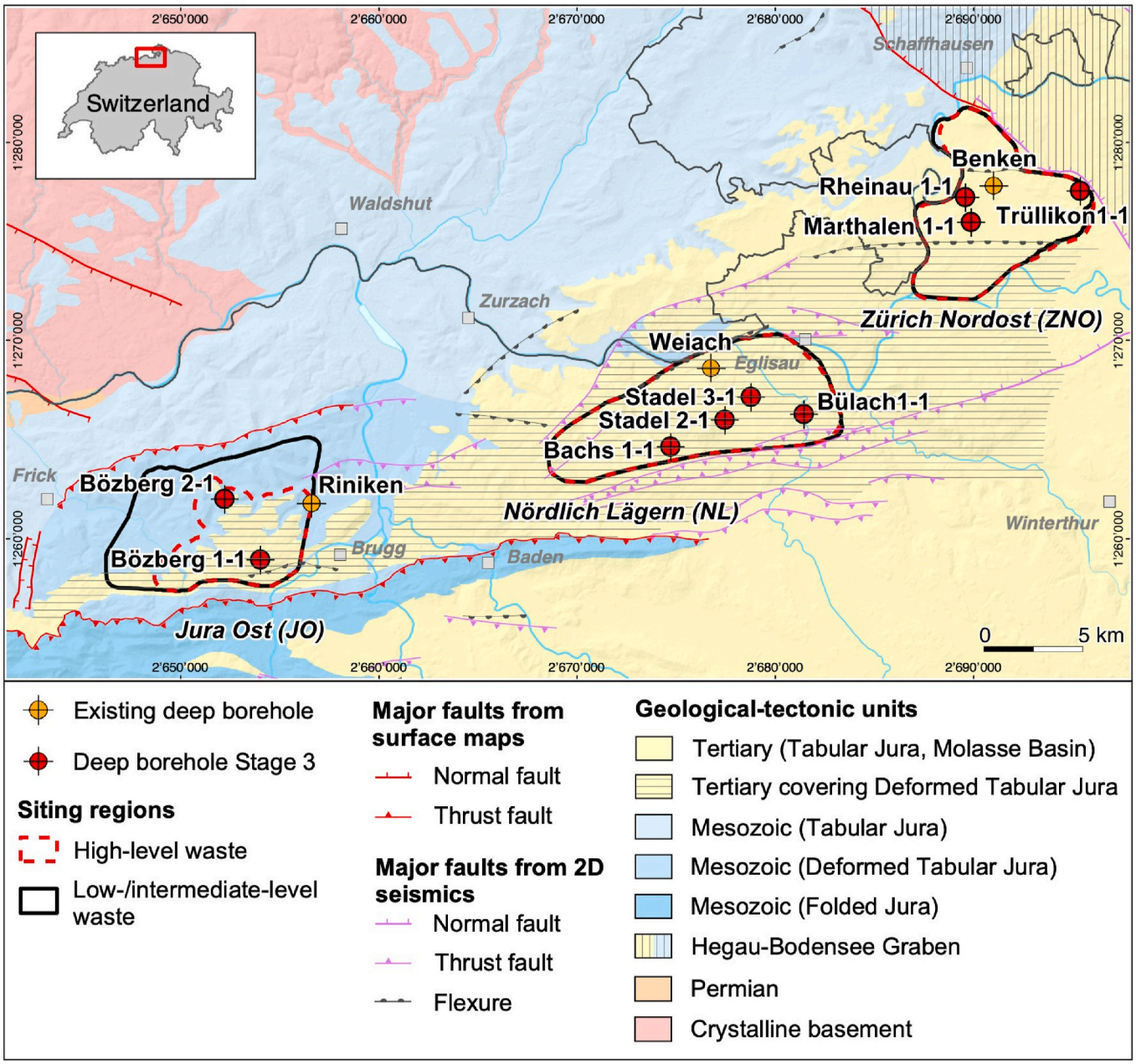

Fig. 1. Geological-tectonic map with locations of study areas and boreholes (adapted from Madritsch 2015).

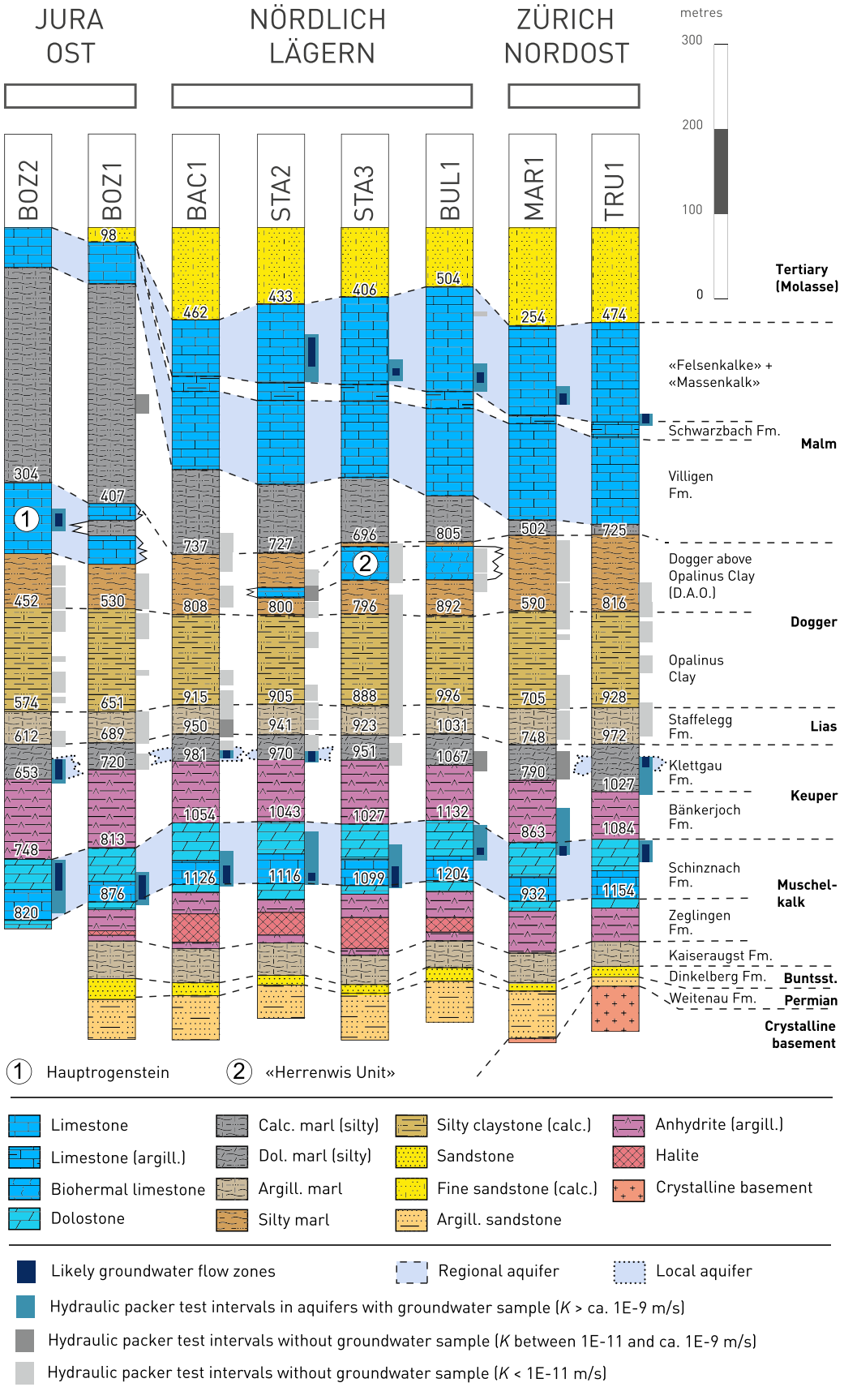

(caption on next page)

Fig. 2. Simplified lithostratigraphic profiles of vertical boreholes drilled in the frame of the deep drilling project in 2019–2022, arranged from W (left) to E (right). Deviated borehole Rheinau 1-1 is not shown because only a small geochemical programme was performed for this core. Numbers indicate depths of selected stratigraphic boundaries in m below surface Note that no hydraulic testing was performed in the Buntsandstein/crystalline basement and in the Tertiary Molasse sections, both of which may include horizons with enhanced permeability.

sampling. Because porewater studies as described in this Special Issue were one of the main objectives of the drilling campaign, a massive on-site infrastructure was set up to seal core samples within minutes after retrieval, in order to minimise the effects of evaporation and oxidation (more detail in Rufer and Stockhecke 2021). For each borehole, a publicly available data report summarising and analysing the geological and geochemical investigations is available (Bülach-1-1: Mazurek et al., 2021; Trüllikon-1-1: Aschwanden et al., 2021; Marthalen-1-1: Mäder et al., 2021; Bözberg-1-1: Wersin et al., 2022; Bözberg-2-1: Gimmi et al., 2022; Stadel-3-1: Aschwanden et al., 2022; Stadel-2-1: Zwahlen et al., 2022; Bachs-1-1: Gaucher et al., 2023). Deviated borehole Rheinau-1-1 was drilled mainly with the objective to penetrate a fault suspected on the basis of 3D seismics, and the geochemical programme was limited to a profile of water-isotope data (Iannotta et al., 2023).

1.2. Geochemical investigation programme

The long-term safety of a deep geological repository relies on multiple lines of evidence that constrain the evolution of the repository system over 1 Myr, the time period of interest for high-level radioactive waste (NEA 2009). A good understanding of the chemical and isotopic compositions of ground- and porewaters provides numerous qualitative and quantitative arguments pertinent to water flow and solute transport in the region of interest. In particular, porewaters in low-permeability, often clay-rich rocks constitute geochemical archives with a memory that is much longer than that of dynamic groundwater systems in aquifers. The spatial distribution of porewater constituents, such as the conservative tracers Cl^-, Br^-, $\delta^{18}O$, δ^2H and noble gases (He, $^3He/^4He$, Ar, $^{40}Ar/^{36}Ar$), inform about the provenance and residence time of the porewaters. A substantial number of tracer profiles across low-permeability sequences worldwide have been subjected to transport modelling, in most cases leading to the conclusion that diffusion is the dominating transport process (Patriarche et al. 2004a, 2004b, Gimmi et al., 2007, Mazurek et al., 2009, 2011, Bensenouci et al., 2011, 2013, Clark et al., 2013, Wersin et al., 2016, 2018, Yu et al., 2018). Such calculations also provided estimates for the evolution times of the currently observed profiles, which were found to vary between several kyr to several Myr, depending on the regional setting. This type of information constitutes natural self-analogues of the sites of interest, i.e. descriptions of the geochemical behaviour at the spatial and temporal scale needed for a safety case.

In this context, investigations pertinent to the understanding of porewater chemistry in the low-permeability sequence were a high priority in the frame of the Swiss deep drilling programme and were accompanied by studies related to the characterisation of the rock materials (e.g. mineralogy, porosity, microfabric, transport properties) and groundwaters that constitute the boundaries of the low-permeability sequence (details in Table 1). A documentation of the applied methods is provided in RWI (2020).

1.3. Structure and contents of the Special Issue

The work presented in this Special Issue pertains to features and processes that occur over a wide range of scales. Fig. 3 provides an overview of the role of each contribution within the overall topic. The studied low-permeability sequence, sandwiched between the Malm and the Triassic aquifers (see Fig. 2), is in general clay-rich but nevertheless lithologically diverse, which also means that transport parameters (porosity, permeability, diffusivity) vary widely. In order to understand and to model profiles of porewater tracers (water isotopes: Gimmi et al., 2023; anions: Wersin et al., 2023; noble gases: Rufer et al., 2023), a good understanding of the rocks and their pore-space architecture is essential. To date, tracer profiles have often been modelled using one single set (or a small number of sets) of transport parameters, mostly due to the scarcity of lithology-specific data (e.g. Gimmi et al., 2007; Mazurek et al., 2011). Given the substantial amount of pertinent data obtained from the borehole profiles studied here, a more detailed and accurate data base of rock properties is available for transport modelling. It includes mineralogical composition, porosity, pore-size distribution and other petrophysical parameters (this paper; Table 1), cation-exchange data (Marques Fernandes et al., 2023) and diffusion coefficients (Van Loon et al., 2023).

Table 1
Overview of the analytical programme pertinent to geochemical investigations.

	Bözberg BOZ2-1	Bözberg BOZ1-1	Bachs BAC1-1	Stadel STA2-1	Stadel STA3-1	Bülach BUL1-1	Marthalen MAR1-1	Rheinau RHE1-1	Trüllikon TRU1-1	Sum
Bulk mineralogy	110	200	86	91	111	206	142	0	146	1092
Mineralogy of the clay fraction	35	55	38	31	39	65	44	0	54	361
Bulk wet density	82	122	76	100	112	123	94	0	67	776
Grain density	102	156	77	97	96	180	109	0	148	965
Gravimetric water content	140	174	94	149	120	179	149	0	151	1156
External surface area (BET) and N_2 ad/desorption isotherm	14	56	11	17	17	56	17	0	36	224
Aqueous extraction	62	104	81	86	90	111	86	0	71	691
Cation exchange capacity (Ni-en method)	3	6	10	3	3	18	7	0	4	54
Cation-exchange capacity (CsCl method, PSI)	10	30	0	19	20	21	20	0	11	131
Porewater composition by squeezing	4	10	0	4	4	10	9	0	13	60
Porewater composition by advective displacement	1	4	6	1	2	5	5	0	3	27
Water isotopes by isotope diffusive exchange	80	103	73	83	97	120	80	51	65	752
Dissolved noble gases	23	34	0	0	29	19	31	0	17	153
Diffusion coefficients for HTO,^{36}Cl and^{22}Na (PSI)	5	33	0	12	7	29	8	0	30	124
Groundwater samples	3	1	2	3	2	2	2	0	3	18

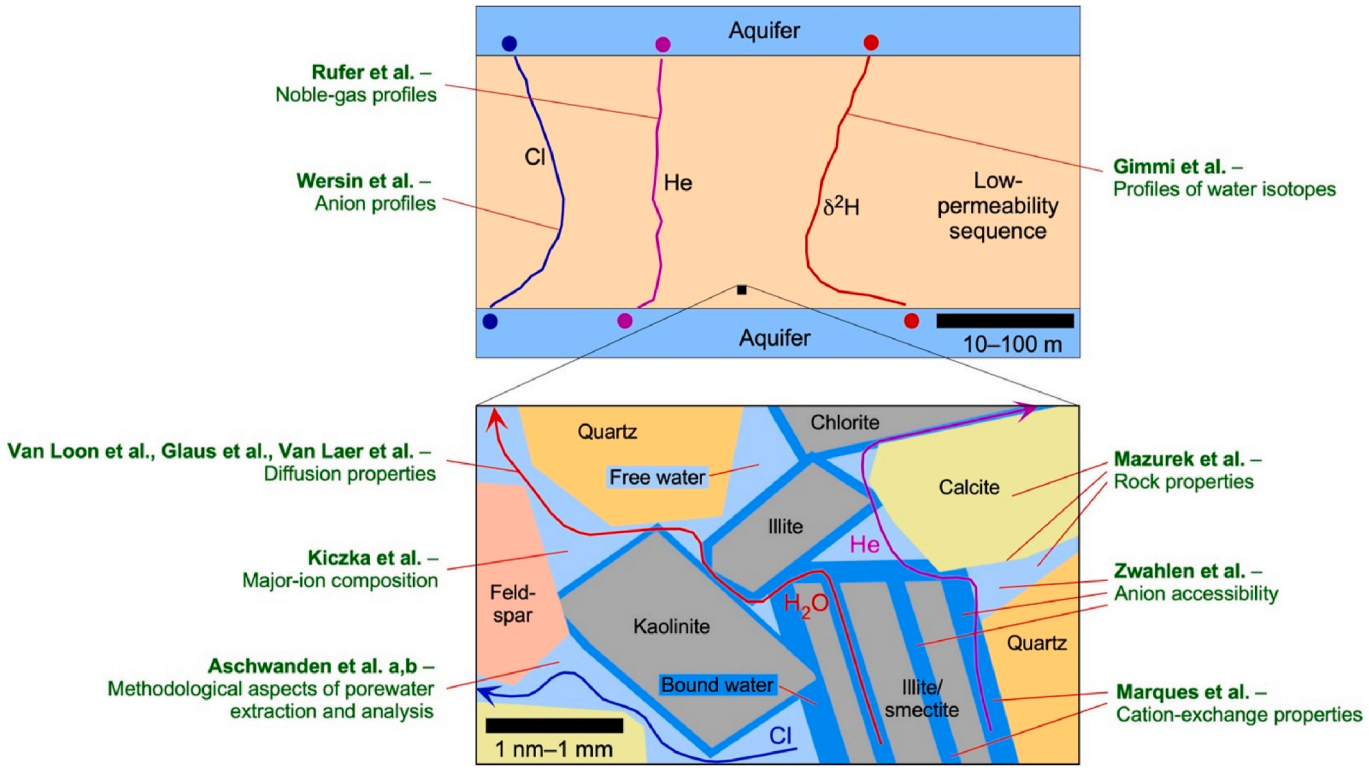

Fig. 3. Conceptual view of features and processes pertinent to the understanding of mineral-porewater-solute interactions and transport phenomena in the studied low-permeability sequence. Note that both sketches are schematic abstractions, and in particular the lower illustration covers a range of scales, given the fact that the bound, anion-depleted water layer has a thickness in the order of 1 nm, while the grain size of calcite and quartz is more likely in the range of μm to mm. References to publications in the Special Issue are given in green.

Many established investigation methods fail or need adaptations when exploring low-porosity rocks with a nanometric pore-space architecture. Thus, some contributions to this Special Issue focus on methodological aspects that are necessary pre-requisites for a successful characterisation of the porewaters:

- The isotope diffusive exchange method is the preferred approach to quantify the stable-isotopic composition of porewater (Rogge 1997; Rübel et al., 2002). It works well for claystones but comes to its limits in heterogeneous and/or low-porosity rocks, such as limestones or evaporites. Aschwanden et al. (2023a) present a new approach to evaluate the experimental results and to better constrain in-situ isotope compositions.
- Aqueous extraction is the simplest method to determine concentrations of conservative constituents, such as Cl^- and Br^-, in bulk porewater. Because anions are repelled from negatively charged clay-mineral surfaces, anion inventories are heterogeneous across a pore. An anion-exclusion factor is thus needed to obtain free-water concentrations (Pearson 1999). To date, many studies used a value for anion accessibility of around 0.5 for clay-rich rocks (Pearson et al., 2003; Mazurek et al., 2009, 2011; Wersin et al., 2016). Based on a data set of unprecedented size, Zwahlen et al. (2023) explore the rock properties that affect anion exclusion and extend the discussion towards clay-poor rocks that are also present in the studied profile. Clay content (defined here as the content of sheet-silicate minerals with grain sizes of less than a few μm) is an important but not the only determining factor. Glaus et al. (2023) pursue an alternative avenue to this end and present a study based on double-layer theory to model laboratory through-diffusion experiments.
- In contrast to Cl^- and Br^-, SO_4^{2-} obtained from aqueous extracts yield porewater concentrations that exceed those obtained from other methods by a factor of around 3–4 (e.g. Mazurek et al., 2012; Wersin et al., 2017). Aschwanden et al. (2023b) apply a suite of protocols to explore potential SO_4^{2-} sources in the rock that could be mobilised during extraction.

Diffusion has been identified as the dominating transport mechanism in the low-permeability sequence in northern Switzerland (Gimmi et al., 2007; Wersin et al., 2018) and elsewhere (e.g. Mazurek et al., 2011; Bensenouci et al., 2011, 2013, 2014; Clark et al., 2013). In order to quantify solute transport, Van Loon et al. (2023) conducted experiments to measure diffusion coefficients for HTO, ^{36}Cl and ^{22}Na. Given the substantial size of the data set, the dependence of diffusion coefficients on lithology could be explored, and formation-specific coefficients were obtained. Further, the experiments also yielded tracer-specific porosities and so constitute one of the main data sources to estimate the anion-accessible porosity fraction. The diffusion data of ^{22}Na represent a broad basis to estimate surface diffusion effects of cationic species in such media. Glaus et al. (2023) propose a pragmatic approach to simultaneously model the diffusion data of anionic and cationic species using an implementation of the electrical double-layer theory. In a related study, Van Laer et al. (2023) compared the diffusion coefficients of selected rock samples obtained by two different laboratories and distinct approaches of raw-data evaluation.

The detailed characterisation of transport parameters in the studied sequence is the basis for solute-transport models. With the free-water concentrations of Cl^- and Br^- at hand, the concentration profiles across the low-permeability sequence were evaluated by Wersin et al. (2023). Data from aqueous extraction were augmented by those from direct sampling techniques, such as squeezing (Mazurek et al., 2015) and advective displacement (Mäder 2018). Simple model calculations explored the diffusive interactions between porewater and the embedding aquifer waters. A similar approach was pursued for water isotopes, with the advantage that these do not depend on porosity and are also not

affected by repulsion by charged clay surfaces (Fig. 3). Evaluation and modelling of these data is the topic of Gimmi et al. (2023). Apart from anions (Cl^- and Br^-) and water isotopes, dissolved noble gases are another group of conservative tracers that can be used to explore the transport processes and the palaeo-hydrogeological evolution. Core samples for the analysis of He contents and $^3He/^4He$ ratios were conditioned immediately on site, in order to minimise artefacts due to outgassing (Rufer and Stockhecke 2021). The substantial dataset is evaluated in Rufer et al. (2023).

Rock squeezing and advective-displacement experiments are the only methods that provide quantitative information on the concentrations of non-conservative solutes, such as cations and SO_4^{2-}, in porewaters of clay-rich drillcore materials. In the ideal case, they provide full major-ion compositions and water-isotope ratios. These methods are evaluated and compared in Kiczka et al. (2023). Vertical and lateral variations of porewater compositions are then discussed in a regional context.

Cation-exchange properties are essential components of a quantification of solute transport, and a decent dataset has been produced by Marques Fernandes et al. (2023). Three different methods (two using Ni-en and one using Cs as selective cation) were applied and compared. Cation-exchange data are the basis to quantify the cation population on the clay exchanger, which in turn is an important constraint for the estimation of the porewater composition by geochemical modelling.

2. Objectives of this introductory paper

Apart from the general presentation of the Swiss deep drilling campaign and of the contents of the Special Issue, this contribution focuses on the characterisation of selected rock properties, given the fact that mineralogy (in particular clay content and clay type), porosity and rock fabric govern many physico-chemical rock characteristics and also the interactions with porewater. Microfabric and pore-space architecture in the various lithologies determine, among others, the transport properties (including anion accessibility of the pore space) and so are also key aspects.

The pore space of clay-rich rocks is dominated by pore sizes in the range of nanometres and so cannot be imaged directly. While a number of studies are available based on BIB-SEM or FIB-SEM, these methods can only image the largest pores, typically <20–30% of the total pore space (Keller et al., 2011; Houben et al., 2013, 2014; Klaver et al., 2015). TEM and STEM techniques provide a better resolution (e.g. Curtis et al., 2011, Keller et al., 2013) but the upscaling of the information to the hand-specimen or even formation scale remains an issue. Here, we utilise N_2 ad-/desorption isotherms to obtain pore-size distributions and interpret the data in conjunction with other rock parameters.

3. Geological and hydrogeological setting

The three study areas are located N to NE of the Folded Jura, a Mio-to Pliocene thin-skinned fold-and-thrust belt related to the late stages of Alpine shortening (Fig. 1; Laubscher 1972; Becker 2000; Madritsch 2015). Here, the Mesozoic sequence is flat-lying, with a dip of about 4° towards SE. Areas Jura Ost (JO) and Nördlich Lägern (NL) are located in the Deformed Tabular Jura, a zone beyond the frontal thrust of the Folded Jura but still affected by compressional tectonics, featured by several WSW-ENE-striking thrust faults that separate flat-lying, essentially undeformed blocks (Malz et al., 2019). While the southernmost part of the Zürich Nordost (ZNO) area is also affected by compressional tectonics, the larger part is situated within the undeformed Tabular Jura. Towards the NE, this area is bounded by a regional, NW-SE trending normal fault that separates the Tabular Jura from the Hegau-Bodensee Graben, a Cenozoic rift system (Egli et al., 2016; Ring and Gerdes 2016).

The basement (either crystalline or Permian sedimentary rocks) is overlain by a heterogeneous sequence of Triassic units of predominantly shallow marine, coastal or continental facies, including evaporitic beds (dolostone, anhydrite, halite). Open marine conditions prevailed since the onset of the Liassic until the upper Jurassic (Malm), and the rocks consist of mixtures of continental clastic input (claystones, silt/sandstones) and marine carbonates in various proportions. The massive limestones of the Malm were affected by erosion and karstification in consequence of basin inversion during the late Cretaceous and are discordantly overlain by Tertiary Molasse deposits.

In contrast to many other Jurassic units, the 100–120 m thick Opalinus Clay is laterally continuous, with only minor facies changes. The subdivision into 4 sub-units as proposed by Mazurek and Aschwanden (2019) is found consistently throughout the region of interest. In contrast, the Dogger units overlying the Opalinus Clay show substantial lateral heterogeneity. In the Zürich-Nordost area (ZNO), clay-rich units dominate. The same is true for the Nördlich Lägern area (NL), with the exception of a massive, up to 40 m thick coral reef (Herrenwis Unit) that is present in the eastern part of this study area. Towards the west, a drastic change towards calcareous lithologies is observed in the Jura Ost area (JO), where partly oolitic limestone (Hauptrogenstein) constitutes the lateral equivalent. Over the whole region, the overlying Malm is dominated by massive limestones and calcareous marls. In the Jurassic, a substantial number of horizons with slow or absent sedimentation are found. These condensed horizons consist of hardgrounds and Fe-rich oolites, whose microfabric and pore-space architecture differ substantially from that of other rocks (see below).

Regional or local aquifers constitute the boundaries of the low-permeability sequence and are shown in Fig. 2, and hydraulic data are documented in Schwarz et al. (2021a, b, c, 2022a, b, c, d, 2023). In areas NL and ZNO, the Malm aquifer forms the upper boundary of the low-permeability sequence and is hosted by fractured and karstified massive limestone. Hydraulic conductivity based on packer testing is moderate and lies in the range 1×10^{-9}–4×10^{-8} m/s. In the most western area (JO), the Hauptrogenstein, an oolitic limestone located in the upper Dogger, represents the upper boundary in borehole BOZ2-1 ($K = 1\times10^{-8}$ m/s), while its hydraulic conductivity is low in borehole BOZ1-1. The lower boundary is located either in the Keuper or in the Muschelkalk aquifer (Fig. 2). The Keuper aquifer is lithologically and hydraulically heterogeneous and, if present, hosted by sandstones or dolostones. Its hydraulic conductivity varies over a wide range (max. 6×10^{-6} m/s), but in some boreholes it cannot be considered to constitute an aquifer defining the lower boundary because its hydraulic conductivity is too low. In contrast, the underlying Muschelkalk aquifer, hosted by porous dolostone, is of regional extent with typically high hydraulic conductivity (3×10^{-8}–3×10^{-6} m/s). The Keuper and Muschelkalk aquifers are separated by evaporitic, anhydrite-bearing beds with extremely low hydraulic conductivites. The resulting thickness of the low-permeability sequence with the Opalinus Clay in its centre thus is ≥ 390 m (ZNO), ≥410 m (NL) and ≥260 m (JO).

4. Results of rock studies

4.1. Lithology and mineralogy

The Jurassic part of the drilled profile is dominated by clastic and biogenic constituents, i.e. by clay minerals, quartz and carbonates (mostly calcite) in widely variable proportions. The degree of dolomitisation is in general limited (mean dolomite/carbonate = 0.03 in mass units), with exceptionally high values of up to 0.56 in some carbonate-poor units, in particular the Frick Mb. of the Liassic Staffelegg Fm. Unit-specific averages and standard deviations for the mineralogical composition are listed in Table 2. Given its high degree of lithological homogeneity, all data for the Opalinus Clay are lumped together, while thinner but lithologically more heterogeneous units, such as the Liassic Staffelegg Fm. or the Dogger above Opalinus Clay (D.A.O.), are further subdivided into sub-units. Fe-rich oolites, which occur at different stratigraphic levels in the Dogger above Opalinus Clay, are lumped and

Table 2
Mineralogical composition (average±1σ in wt.%) of selected Jurassic units in the three study areas. No. = number of samples, b.d. = below detection. The Rietheim Mb. of the Staffelegg Fm. is better known as the Posidonia Shale. Dolomite may include an ankeritic component.

Area	Unit	No.	Clay minerals	Quartz	K-feldspar	Plagioclase	Calcite	Dolomite	Siderite	Goethite	Pyrite	C(org)
JO	Wildegg Fm.	25	20.9 ± 9.4	7.1 ± 3.3	2.3 ± 1.6	0.3 ± 0.5	67.3 ± 14.1	1.5 ± 1.7	b.d.	b.d.	0.3 ± 0.3	0.4 ± 0.1
JO	Fe-rich oolites	10	23.4 ± 10.2	5.5 ± 4.1	0.9 ± 1.3	0.1 ± 0.3	59.9 ± 18.4	3.8 ± 4.4	b.d.	5.2 ± 6.1	0.6 ± 0.6	0.4 ± 0.3
JO	Hauptrogenstein excl. Fe-ool.	22	18.8 ± 10.2	5.4 ± 4.5	0.8 ± 1.4	0.3 ± 0.7	69.5 ± 14.6	4.2 ± 4.0	b.d.	b.d.	0.6 ± 0.6	0.5 ± 0.3
JO	Passwang Fm. excl. Fe-ool.	48	38.3 ± 10.5	26.0 ± 9.0	4.4 ± 1.4	2.7 ± 1.2	26.1 ± 15.1	0.4 ± 1.4	b.d.	b.d.	1.4 ± 0.8	0.7 ± 0.2
JO	Opalinus Clay	94	57.3 ± 10.2	21.8 ± 5.4	3.9 ± 1.5	2.6 ± 0.7	9.7 ± 6.5	0.2 ± 0.8	2.8 ± 2.6	b.d.	0.7 ± 0.7	1.0 ± 0.3
JO	Staffelegg Fm., Gross Wolf Mb.	1	26.8	5.6	3.0	1.4	54.1	8.0	0.9	b.d.	b.d.	0.3
JO	Staffelegg Fm., Rietheim Mb.	3	46.6 ± 4.8	11.3 ± 2.0	3.0 ± 0.5	1.7 ± 0.4	27.0 ± 10.8	1.1 ± 1.0	b.d.	0.3 ± 0.6	3.8 ± 2.2	5.2 ± 2.3
JO	Staffelegg Fm., Frick Mb.	19	38.0 ± 9.7	39.0 ± 8.7	4.8 ± 1.6	2.6 ± 0.5	10.3 ± 4.8	3.6 ± 2.9	b.d.	b.d.	1.0 ± 0.8	0.6 ± 0.1
JO	Staffelegg Fm., Beggingen Mb.	1	6.7	0.8	b.d.	b.d.	82.6	9.6	b.d.	b.d.	b.d.	0.2
JO	Staffelegg Fm., Schambelen Mb.	10	66.5 ± 7.9	12.6 ± 4.4	3.4 ± 1.6	1.3 ± 0.7	12.4 ± 8.4	0.1 ± 0.3	b.d.	b.d.	2.8 ± 2.2	0.9 ± 0.5
NL	Felsenkalke/Massenkalk	18	2.0 ± 1.4	0.2 ± 0.4	b.d.	b.d.	97.8 ± 1.6	b.d.	b.d.	b.d.	b.d.	0.1 ± 0.1
NL	Villigen Fm.	14	7.0 ± 4.2	1.0 ± 1.1	0.1 ± 0.5	b.d.	91.0 ± 5.7	0.6 ± 1.0	b.d.	b.d.	0.1 ± 0.1	0.2 ± 0.1
NL	Wildegg Fm.	37	22.9 ± 6.8	6.9 ± 3.6	2.4 ± 1.3	0.5 ± 1.0	65.1 ± 10.4	1.6 ± 1.7	b.d.	b.d.	0.2 ± 0.1	0.4 ± 0.2
NL	Fe-rich oolites	20	41.2 ± 21.1	24.5 ± 17.6	3.2 ± 2.3	2.1 ± 1.5	21.0 ± 25.9	2.2 ± 4.4	0.3 ± 0.6	3.8 ± 9.5	0.7 ± 0.5	0.5 ± 0.3
NL	Variansmergel Fm.	4	58.5 ± 5.5	15.7 ± 0.9	4.5 ± 2.0	1.7 ± 0.4	15.2 ± 5.3	2.7 ± 3.2	b.d.	b.d.	1.2 ± 0.5	0.5 ± 0.1
NL	Parkinsoni-Württembergica Sch.	26	49.3 ± 9.4	18.6 ± 4.5	4.1 ± 2.3	2.3 ± 1.4	22.4 ± 7.1	1.3 ± 1.5	0.1 ± 0.7	b.d.	1.1 ± 0.8	0.7 ± 0.2
NL	Herrenwis Unit	33	13.2 ± 15.9	6.9 ± 7.6	1.4 ± 1.9	0.4 ± 1.0	74.7 ± 24.5	2.8 ± 4.2	b.d.	b.d.	0.3 ± 0.6	0.3 ± 0.2
NL	Wedelsandstein Fm.	36	41.6 ± 15.1	29.9 ± 7.3	5.2 ± 1.5	3.0 ± 0.8	17.8 ± 11.4	0.1 ± 0.3	0.7 ± 1.5	b.d.	1.0 ± 0.7	0.6 ± 0.2
NL	Opalinus Clay	144	56.3 ± 10.0	22.8 ± 6.5	4.4 ± 1.4	2.8 ± 0.7	8.6 ± 5.9	b.d.	3.3 ± 2.0	b.d.	0.7 ± 0.8	1.0 ± 0.2
NL	Staffelegg Fm., Gross Wolf Mb.	3	18.1 ± 4.3	3.6 ± 0.4	1.4 ± 1.3	0.4 ± 0.6	75.6 ± 4.8	0.5 ± 0.9	b.d.	b.d.	b.d.	0.4 ± 0.1
NL	Staffelegg Fm., Rietheim Mb.	11	37.1 ± 7.0	9.2 ± 1.8	2.7 ± 1.2	2.0 ± 1.0	40.5 ± 12.2	0.8 ± 1.5	b.d.	b.d.	2.6 ± 1.3	4.9 ± 1.5
NL	Staffelegg Fm., Frick Mb.	26	41.8 ± 6.5	38.8 ± 6.2	4.9 ± 1.2	3.0 ± 0.6	8.5 ± 4.0	1.5 ± 1.1	0.2 ± 0.5	b.d.	0.6 ± 0.3	0.7 ± 0.2
NL	Staffelegg Fm., Beggingen Mb.	1	7.5	1.5	b.d.	b.d.	90.5	b.d.	b.d.	b.d.	0.2	0.3
NL	Staffelegg Fm., Schambelen Mb.	8	41.8 ± 20.9	19.7 ± 9.8	3.4 ± 1.7	1.3 ± 1.3	32.4 ± 25.4	0.4 ± 0.9	b.d.	b.d.	0.6 ± 0.4	0.4 ± 0.1
ZNO	Felsenkalke/Massenkalk	7	2.7 ± 3.5	1.0 ± 1.2	0.2 ± 0.5	b.d.	94.5 ± 6.4	1.5 ± 2.9	b.d.	b.d.	b.d.	0.2 ± 0.1
ZNO	Villigen Fm.	7	5.3 ± 2.4	0.8 ± 1.0	0.3 ± 0.7	b.d.	92.7 ± 4.3	0.6 ± 1.0	b.d.	b.d.	b.d.	0.2 ± 0.1
ZNO	Wildegg Fm.	5	24.2 ± 8.2	6.2 ± 2.6	3.2 ± 0.8	0.7 ± 0.6	61.5 ± 12.4	3.6 ± 3.7	b.d.	b.d.	0.3 ± 0.3	0.4 ± 0.1
ZNO	Fe-rich oolites	5	29.0 ± 14.9	25.4 ± 10.9	4.0 ± 1.4	1.8 ± 1.4	37.0 ± 27.4	1.3 ± 2.3	0.3 ± 0.4	b.d.	0.6 ± 0.6	0.6 ± 0.4
ZNO	Variansmergel Fm.	12	46.0 ± 13.9	20.2 ± 4.6	4.1 ± 2.3	1.9 ± 1.2	24.5 ± 13.0	1.1 ± 1.8	0.2 ± 0.4	b.d.	1.2 ± 0.4	0.8 ± 0.3
ZNO	Parkinsoni-Württembergica Sch.	25	43.2 ± 10.0	19.8 ± 4.7	5.5 ± 1.0	2.2 ± 0.8	25.4 ± 10.4	1.8 ± 1.5	0.2 ± 0.5	b.d.	1.2 ± 0.6	0.7 ± 0.2
ZNO	Wedelsandstein Fm.	35	31.0 ± 13.6	38.1 ± 10.3	5.9 ± 1.2	3.2 ± 0.9	20.2 ± 11.3	0.3 ± 0.6	b.d.	b.d.	0.8 ± 0.5	0.6 ± 0.2
ZNO	Opalinus Clay	101	56.8 ± 6.2	22.0 ± 4.2	5.0 ± 1.0	2.9 ± 0.8	8.3 ± 3.2	b.d.	3.1 ± 2.1	b.d.	0.7 ± 0.5	1.1 ± 0.2
ZNO	Staffelegg Fm., Gross Wolf Mb.	3	32.8 ± 5.4	7.0 ± 1.0	2.8 ± 0.5	2.0 ± 0.4	52.2 ± 5.4	1.8 ± 1.6	0.7 ± 0.6	b.d.	0.2 ± 0.1	0.5 ± 0.2
ZNO	Staffelegg Fm., Rietheim Mb.	10	39.1 ± 5.5	10.6 ± 2.8	2.8 ± 0.9	1.6 ± 0.8	37.2 ± 12.3	0.5 ± 0.8	0.2 ± 0.4	b.d.	2.9 ± 2.0	5.0 ± 1.6
ZNO	Staffelegg Fm., Frick Mb.	11	55.6 ± 10.0	26.1 ± 9.5	5.0 ± 1.0	3.0 ± 0.6	6.8 ± 1.9	0.7 ± 1.1	1.4 ± 1.5	b.d.	0.5 ± 0.3	0.9 ± 0.1
ZNO	Staffelegg Fm., Beggingen Mb.	4	58.1 ± 31.3	15.4 ± 9.8	1.9 ± 2.2	1.2 ± 1.3	21.5 ± 42.4	b.d.	0.6 ± 1.2	b.d.	0.7 ± 0.4	0.6 ± 0.3
ZNO	Staffelegg Fm., Schambelen Mb.	3	64.1 ± 5.9	27.0 ± 7.7	3.4 ± 3.0	1.3 ± 1.2	2.6 ± 0.3	b.d.	b.d.	b.d.	0.9 ± 0.1	0.6 ± 0.1

reported as one unit. Note that while the 5 Fe-rich oolite samples taken in the ZNO area do not contain goethite, goethite-bearing beds nevertheless occur but were not sampled. The underlying Triassic is more heterogeneous and contains, among others, massive dolostone and anhydrite-rich units. The Zeglingen Fm. below the Muschelkalk aquifer also contains massive halite in most boreholes except in MAR1-1 and TRU1-1 (Fig. 2). Fig. 4 provides an overview of the mineralogical compositions in the studied profiles, based on XRD analysis of 1092 core samples.

- The Upper Muschelkalk consists of porous dolostones throughout the region and hosts the regional Muschelkalk aquifer (Aschwanden et al. 2019a, 2019b). The overlying Keuper is lithologically heterogeneous. Its lower part (Bänkerjoch Fm.) contains anhydrite-rich beds that act as top seals of the Muschelkalk aquifer. The upper part (Klettgau Fm.) is lithologically variable on a metre scale (dolostone-sandstone-marl-claystone), reflecting the coastal to continental sedimentary facies in this period. The Keuper aquifer, if present, is hosted by sandy-dolomitic beds within this formation, but the exact stratigraphic level varies among boreholes.
- The relatively thin Lias consists of marine deposits. It is highly heterogeneous in the vertical dimension (claystone-marl-limestone-sandstone) but much less so laterally. It includes, among others, an organic- and pyrite-rich marl internationally known as Posidonia Shale.
- The Opalinus Clay is the most clay-rich unit in the whole sequence (except for some sections within the Staffelegg Fm.) and shows little variability among the study areas. Clay content increases slightly with depth. The occurrence of siderite is limited to this unit, possibly related to the alteration of detrital biotite that occurs in the Opalinus Clay (Lerouge et al., 2014).
- The Dogger above Opalinus Clay (D.A.O., see Fig. 4) is more heterogeneous in both the vertical and horizontal dimensions. In the ZNO area, the lowermost unit is dominated by argillaceous sandstone (Wedelsandstein Fm.), which is overlain by more clay-rich units. In the NL area, the Wedelsandstein Fm. consists of sandy claystone. The major heterogeneity in this area is the overlying Herrenwis Unit, a limestone consisting of reef material and reef debris (Fig. 2). It is thickest in the BUL1-1 and STA3-1 boreholes (about 40 m) but becomes thinner in STA2-1 (10 m) and is absent in BAC1-1. Above this horizon, clay-rich units predominate. The sedimentary facies changes substantially towards the west (area JO), which is reflected by distinct lithologies. The lower part mainly consists of marl, sandy claystone and argillaceous siltstone

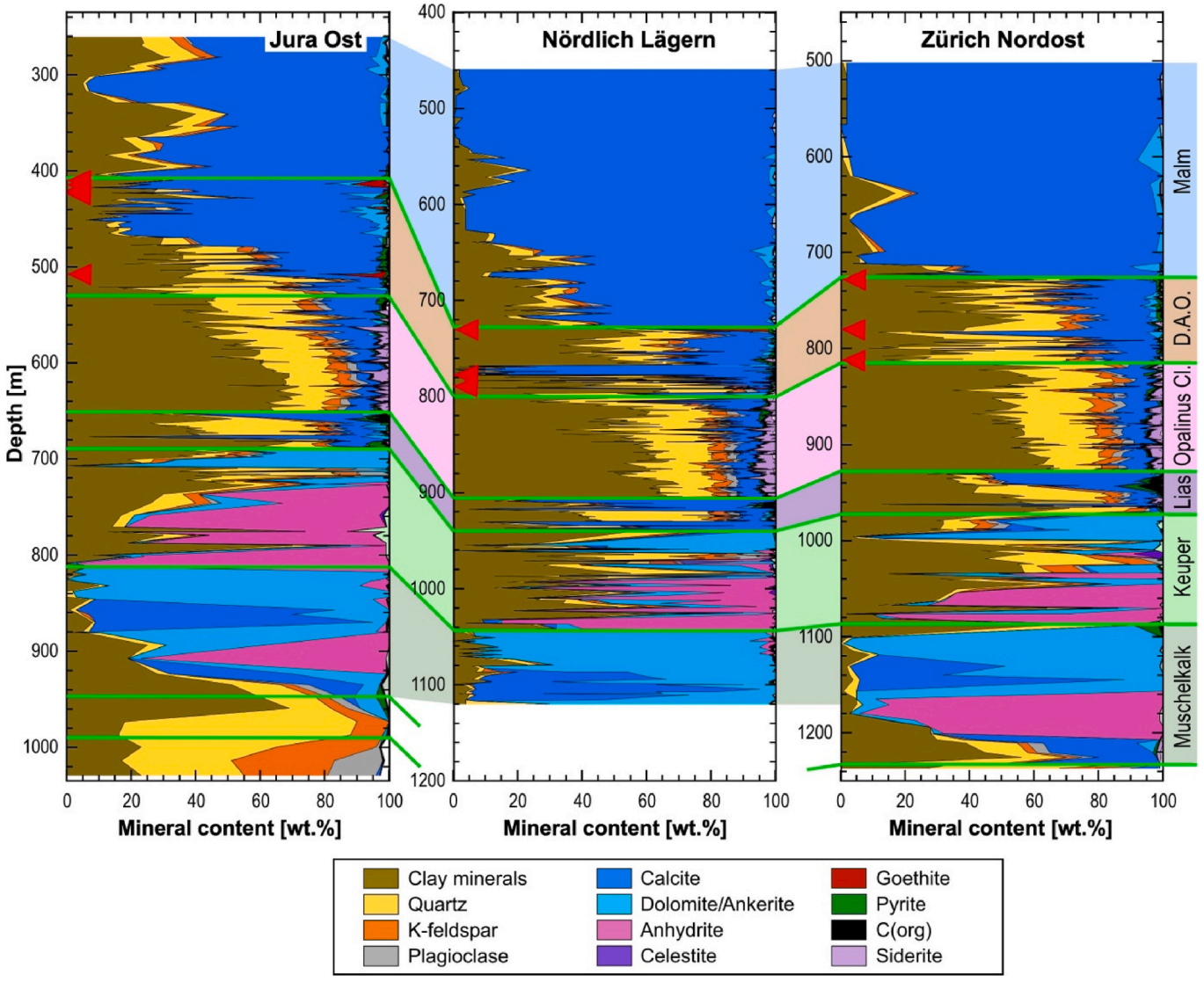

Fig. 4. Mineralogical composition of studied borehole intervals based on laboratory XRD analysis. The formation depths are adjusted to the profiles of BOZ1-1 (JO), STA2-1 (NL) and TRU1-1 (ZNO). D.A.O. = Dogger above Opalinus Clay. Red triangles highlight Fe-rich oolite horizons.

(Passwang Fm.), which is overlain by a thick oolitic limestone (Hauptrogenstein).
- The Malm evolves from marly lithologies towards massive pure limestones throughout the region.

Accessory phases occurring in most formations include pyrite and organic matter. Magnesite was identified in the Triassic evaporites from the Jura Ost area. Celestite was also identified by XRD in evaporites throughout the region. However, SEM investigations indicate the presence of trace amounts of celestite in the Opalinus Clay and possibly other clay-rich formations. Traces of fluorite occur in various units of the Muschelkalk. Goethite and haematite are mainly found in Fe-rich oolites.

Local heterogeneities within the Dogger above Opalinus Clay (D.A.O.) are constituted by condensed horizons reflecting periods of slow or absent deposition. These lithologically heterogeneous and mostly thin (1–15 m) units are typically rich in bioclasts and contain Fe-rich oolites with high concentrations of goethite and minor haematite. In the NL and ZNO areas, they include (from base to top) the Murchisonae Oolith Fm., the Humphriesioolith Fm. and the Wutach Fm., and these are marked by red triangles in Fig. 4. In the JO area, Fe-rich oolites are also found at similar stratigraphic positions. Fe-rich oolites have particular microfabrics and pore-space architecture, which also affects the accessibility of the pore space for anions (further discussed in Zwahlen et al., 2023). They are further addressed in the Discussion section below.

Clay minerals include illite, predominanty illite-rich illite/smectite mixed layers, kaolinite, chlorite and chlorite-rich chlorite/smectite mixed layers. The composition of the clay fraction is shown in Fig. 5, expressed as end-member compositions (i.e. the illite, smectite and chlorite components in mixed-layer phases are attributed to the respective pure minerals). Illite is the dominating clay mineral throughout the profile. This is particularly so in the upper Keuper. In the Lias, the proportions of smectite and chlorite show little variability, while the ratio illite/kaolinite shows some systematic trends, in particular the decrease in the uppermost few metres. The Opalinus Clay has the lowest illite/kaolinite ratio, with a slightly increasing trend towards the top. Smectite and chlorite show remarkably constant contents in both the vertical and lateral dimensions. More scatter and regional heterogeneity is observed in the Dogger above Opalinus Clay. The illite/kaolinite ratio increases towards the top except in the JO area where the opposite is the case, highlighting the contrasting depositional environments during this period. In the NL area, the reef limestones of the Herrenwis Unit (depth interval 767–778 m in Fig. 5) show remarkably high contents of illite and smectite, whereas kaolinite contents are lower than in any of the other units. More consistent trends among the study areas are again found in the overlying Malm.

4.2. Water content and porosity

Water content and porosity depend mainly on the mineralogical composition and the compaction history. Diagenetic effects, such as cementation or mineral dissolution, are additional factors. Porosity data were obtained from the measurement of mass loss after drying rock samples at 105 °C and from bulk wet and grain densities (see RWI 2020 for formalisms to calculate porosities from measured data). The results of both methods are consistent, indicating that the samples used for mass-loss measurement were saturated at the onset of the experiments. Unit-specific averages and standard deviations of petrophysical parameters are listed in Table 3.

Fig. 6 shows the dependence of porosity on lithology. The graphic is limited to data from the Jurassic because of the lithological heterogeneity in the Triassic (evaporites, dolostone, etc.). Claystones have the highest porosity with an average around 0.13. A substantial decrease of porosity is seen towards the limestone corner where porosity lies around 0.04. It is also noteworthy that the relative scatter of the data is by far largest for limestones, reflecting the wide range of fabrics in these rocks.

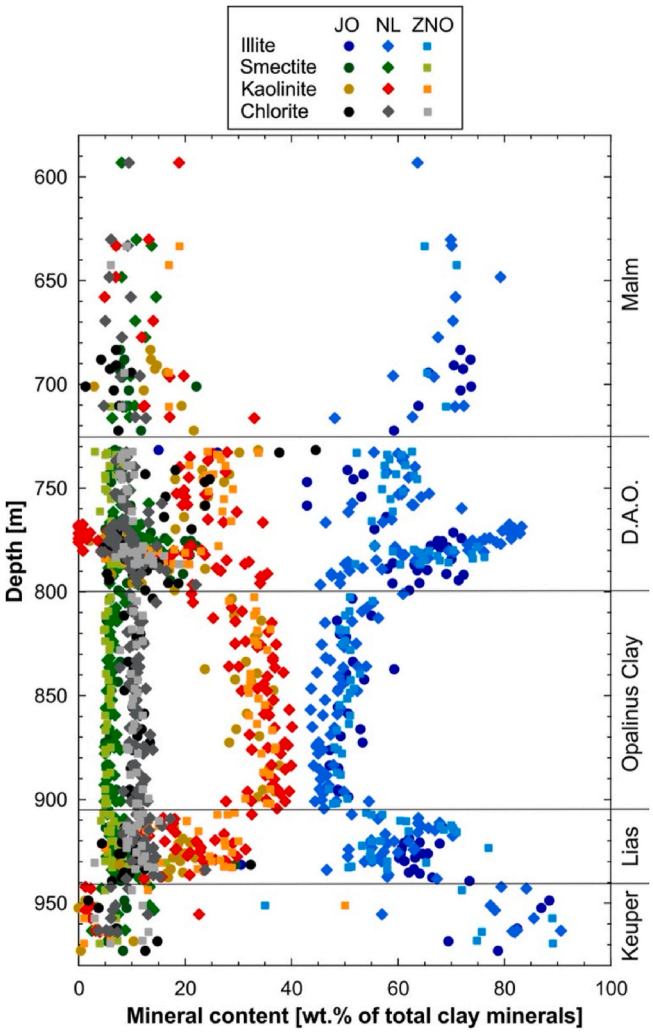

Fig. 5. Composition of the clay fraction (end-member compositions) from all studied boreholes. Depth data are adjusted to the profile of the STA2-1 borehole. D.A.O. = Dogger above Opalinus Clay.

On the other hand, porosity decreases only weakly towards the quartz + feldspars corner (average 0.11).

The vertical distribution of water-content porosity is shown in Fig. 7a. Porosity is low in the Malm limestones and increases towards the base of this unit. On average, it remains high in the Dogger above Opalinus Clay (D.A.O.), but the variability is substantial, reflecting the lithological heterogeneity. A conspicuous drop can be seen in the reef limestones of the Herrenwis Unit that is present in the NL area. In the Opalinus Clay, variability is limited, and a trend towards higher porosity with depth is seen, reflecting the increasing clay content. Variability is highest in the uppermost part that contains silty-calcareous beds. In the Lias, the spread of the data is substantial but systematic (Fig. 7c and d). Some well-defined depth trends can be identified, and discontinuities or breaks in the trends correspond to the boundaries of the stratigraphic members of this unit. The trends in water content mirror those of clay content but are even better defined than the latter. There is a remarkable consistency of the data between boreholes, which illustrates a high degree of lithological homogeneity in the horizontal dimension of the Lias, while heterogeneity is substantial in the vertical dimension. One exception to lateral homogeneity is the Frick Mb., which is markedly more clay-rich in the ZNO area (Fig. 7d). The underlying Triassic is characterised by a large variability of porosity, reflecting the intercalation of lithologies with high porosity, such as claystones, dolostones and sandstones, and those with low porosity, such as anhydrite-rich

Table 3
Petrophysical properties of selected Jurassic units in the three study areas, given as average±1σ (number of samples). Fe-rich oolites in the JO area include the Spatkalk and the Humphriesioolith-Fm. Fe-rich oolites in the NL and ZNO areas include the Wutach Fm., the Humphriesioolith-Fm. and the Murchisonae-Oolith Fm. n.d. = no data. The Rietheim Mb. of the Staffelegg Fm. is internationally known as the Posidonia Shale.

Area	Unit	Bulk wet density [g/cm^3]	Grain density [g/cm^3]	Porosity from densities [–]	Water content (wet) [wt.%]	Water-content porosity [–]	External surface area (BET) [m^2/g$_{dry\ rock}$]	Mean radius of external pores [nm]
JO	Wildegg Fm.	2.593 ± 0.037 (25)	2.703 ± 0.008 (25)	0.069 ± 0.022 (25)	3.092 ± 1.042 (27)	0.079 ± 0.025 (27)	17.5 ± 6.8 (9)	4.10 ± 1.43
JO	Fe-rich oolites	2.559 ± 0.027 (8)	2.768 ± 0.077 (9)	0.116 ± 0.042 (8)	4.429 ± 1.363 (15)	0.112 ± 0.034 (15)	14.0 ± 7.9 (5)	11.00 ± 6.03
JO	Hauptrogenstein excl. Fe-ool.	2.586 ± 0.025 (19)	2.735 ± 0.024 (21)	0.080 ± 0.015 (19)	2.862 ± 0.647 (26)	0.074 ± 0.016 (26)	6.7 ± 0.4 (2)	7.58 ± 0.52
JO	Passwang Fm. excl. Fe-ool.	2.531 ± 0.034 (32)	2.701 ± 0.015 (35)	0.105 ± 0.022 (32)	4.357 ± 1.150 (54)	0.109 ± 0.027 (54)	25.5 ± 5.5 (16)	3.70 ± 0.72
JO	Opalinus Clay	2.517 ± 0.031 (57)	2.702 ± 0.029 (83)	0.112 ± 0.014 (54)	4.705 ± 0.608 (86)	0.117 ± 0.014 (83)	31.4 ± 5.3 (11)	3.37 ± 0.32
JO	Staffelegg Fm., Gross Wolf Mb.	2.586 (1)	2.721 (1)	0.081 (1)	3.479 ± 0.257 (2)	0.089 ± 0.006 (2)	n.d.	n.d.
JO	Staffelegg Fm., Rietheim Mb.	2.400 (1)	2.506 ± 0.035 (3)	0.095 (1)	4.376 ± 0.359 (4)	0.105 ± 0.007 (4)	26.1 ± 8.1 (2)	3.77 ± 0.75
JO	Staffelegg Fm., Frick Mb.	2.529 ± 0.022 (10)	2.691 ± 0.019 (15)	0.095 ± 0.005 (10)	3.788 ± 0.204 (20)	0.096 ± 0.005 (20)	23.3 ± 3.1 (7)	3.38 ± 0.36
JO	Staffelegg Fm., Beggingen Mb.	2.685 (1)	2.747 (1)	0.029 (1)	0.698 (1)	0.019 (1)	1.7 (1)	8.11
JO	Staffelegg Fm., Schambelen Mb.	2.507 ± 0.038 (8)	2.718 ± 0.023 (10)	0.131 ± 0.010 (8)	5.753 ± 0.402 (11)	0.142 ± 0.009 (11)	45.9 ± 2.5 (4)	2.71 ± 0.11
NL	Felsenkalke/Massenkalk	2.679 ± 0.020 (26)	2.716 ± 0.007 (26)	0.019 ± 0.011 (26)	0.527 ± 0.389 (26)	0.014 ± 0.010 (26)	2.1 ± 1.5 (2)	5.58 ± 1.07
NL	Villigen Fm.	2.667 ± 0.027 (24)	2.709 ± 0.008 (25)	0.024 ± 0.014 (24)	0.959 ± 0.580 (27)	0.025 ± 0.015 (27)	8.6 ± 1.6 (3)	2.61 ± 1.10
NL	Wildegg Fm.	2.603 ± 0.029 (32)	2.710 ± 0.008 (34)	0.065 ± 0.015 (30)	2.637 ± 0.705 (37)	0.068 ± 0.017 (37)	13.4 ± 4.2 (6)	2.91 ± 0.84
NL	Fe-rich oolites	2.520 ± 0.061 (17)	2.778 ± 0.156 (17)	0.132 ± 0.060 (14)	5.295 ± 1.809 (23)	0.132 ± 0.047 (23)	25.2 ± 15.5 (5)	8.50 ± 7.72
NL	Variansmergel Fm.	2.501 ± 0.022 (3)	2.726 ± 0.010 (3)	0.134 ± 0.013 (3)	5.837 ± 0.705 (5)	0.144 ± 0.016 (5)	40.8 (1)	3.04
NL	Parkinsoni-Württembergica Sch.	2.514 ± 0.033 (21)	2.711 ± 0.015 (20)	0.118 ± 0.016 (19)	4.839 ± 0.665 (34)	0.120 ± 0.016 (31)	33.3 ± 4.1 (11)	3.30 ± 0.26
NL	Herrenwis Unit	2.641 ± 0.067 (22)	2.726 ± 0.014 (23)	0.051 ± 0.039 (18)	1.510 ± 1.564 (33)	0.039 ± 0.039 (33)	3.5 ± 2.2 (6)	4.85 ± 1.96
NL	Wedelsandstein Fm.	2.520 ± 0.037 (23)	2.702 ± 0.014 (27)	0.112 ± 0.024 (17)	4.606 ± 0.890 (34)	0.115 ± 0.021 (34)	28.0 ± 7.1 (13)	3.49 ± 0.69
NL	Opalinus Clay	2.528 ± 0.026 (87)	2.698 ± 0.016 (123)	0.105 ± 0.014 (84)	4.455 ± 0.550 (145)	0.112 ± 0.013 (142)	29.2 ± 4.4 (16)	3.08 ± 0.21
NL	Staffelegg Fm., Gross Wolf Mb.	2.582 ± 0.017 (5)	2.713 ± 0.006 (3)	0.071 ± 0.013 (3)	2.743 ± 0.671 (6)	0.071 ± 0.017 (6)	10.6 ± 0.9 (2)	4.65 ± 1.86
NL	Staffelegg Fm., Rietheim Mb.	2.384 ± 0.064 (8)	2.554 ± 0.042 (9)	0.099 ± 0.010 (7)	4.362 ± 0.404 (12)	0.106 ± 0.010 (12)	21.2 ± 6.8 (7)	4.65 ± 1.45
NL	Staffelegg Fm., Frick Mb.	2.555 ± 0.016 (16)	2.691 ± 0.007 (17)	0.086 ± 0.007 (14)	3.638 ± 0.295 (29)	0.092 ± 0.007 (29)	23.9 ± 1.8 (13)	3.14 ± 0.34
NL	Staffelegg Fm., Beggingen Mb.	2.629 (1)	2.742 (1)	0.052 (1)	1.127 (1)	0.030 (1)	2.8 (1)	8.29
NL	Staffelegg Fm., Schambelen Mb.	2.559 ± 0.062 (6)	2.722 ± 0.015 (7)	0.094 ± 0.038 (6)	3.850 ± 1.868 (8)	0.097 ± 0.045 (8)	26.4 ± 16.0 (5)	2.86 ± 0.33
ZNO	Felsenkalke/Massenkalk	2.627 ± 0.047 (8)	2.707 ± 0.010 (12)	0.038 ± 0.023 (8)	1.369 ± 0.658 (12)	0.033 ± 0.016 (10)	2.6 (1)	7.19
ZNO	Villigen Fm.	2.655 ± 0.030 (9)	2.712 ± 0.011 (12)	0.028 ± 0.018 (9)	0.952 ± 0.629 (12)	0.021 ± 0.010 (11)	3.1 ± 1.3 (2)	4.75 ± 0.44
ZNO	Wildegg Fm.	2.587 ± 0.052 (5)	2.710 ± 0.010 (5)	0.076 ± 0.027 (5)	3.171 ± 0.862 (5)	0.081 ± 0.021 (5)	26.6 (1)	3.17
ZNO	Fe-rich oolites	2.594 ± 0.016 (2)	2.715 ± 0.004 (3)	0.063 ± 0.008 (2)	3.788 ± 1.602 (5)	0.110 ± 0.026 (4)	30.7 ± 1.6 (2)	3.56 ± 0.12
ZNO	Variansmergel Fm.	2.500 ± 0.065 (5)	2.705 ± 0.021 (9)	0.103 ± 0.034 (4)	4.508 ± 1.355 (12)	0.114 ± 0.033 (10)	28.7 ± 9.5 (2)	3.14 ± 0.28
ZNO	Parkinsoni-Württembergica Sch.	2.501 ± 0.049 (11)	2.704 ± 0.012 (18)	0.116 ± 0.026 (11)	4.724 ± 1.039 (27)	0.118 ± 0.025 (23)	31.3 ± 3.2 (7)	3.39 ± 0.20
ZNO	Wedelsandstein Fm.	2.491 ± 0.064 (13)	2.688 ± 0.016 (25)	0.116 ± 0.023 (12)	4.258 ± 1.157 (30)	0.105 ± 0.029 (27)	17.8 ± 9.0 (11)	4.74 ± 1.31
ZNO	Opalinus Clay	2.508 ± 0.024 (36)	2.690 ± 0.016 (92)	0.110 ± 0.011 (36)	4.487 ± 0.526 (87)	0.114 ± 0.012 (74)	29.3 ± 3.0 (9)	3.07 ± 0.28
ZNO	Staffelegg Fm., Gross Wolf Mb.	2.575 (1)	2.707 ± 0.008 (2)	0.080 (1)	3.193 ± 0.373 (5)	0.082 ± 0.009 (5)	17.4 (1)	3.59
ZNO	Staffelegg Fm., Rietheim Mb.	2.367 ± 0.061 (6)	2.524 ± 0.069 (8)	0.104 ± 0.024 (6)	4.133 ± 0.644 (13)	0.103 ± 0.012 (12)	21.4 ± 5.5 (6)	4.43 ± 1.21
ZNO	Staffelegg Fm., Frick Mb.	2.514 ± 0.038 (6)	2.698 ± 0.017 (9)	0.105 ± 0.015 (6)	4.208 ± 0.439 (14)	0.108 ± 0.009 (12)	31.9 ± 3.2 (4)	2.78 ± 0.23
ZNO	Staffelegg Fm., Beggingen Mb.	2.562 ± 0.112 (3)	2.720 ± 0.030 (3)	0.090 ± 0.059 (3)	4.242 ± 2.471 (4)	0.101 ± 0.073 (3)	23.3 ± 29.2 (2)	3.79 ± 1.24
ZNO	Staffelegg Fm., Schambelen Mb.	2.512 ± 0.006 (2)	2.716 ± 0.016 (3)	0.130 ± 0.003 (2)	4.597 ± 2.274 (5)	0.114 ± 0.056 (5)	43.5 (1)	2.74

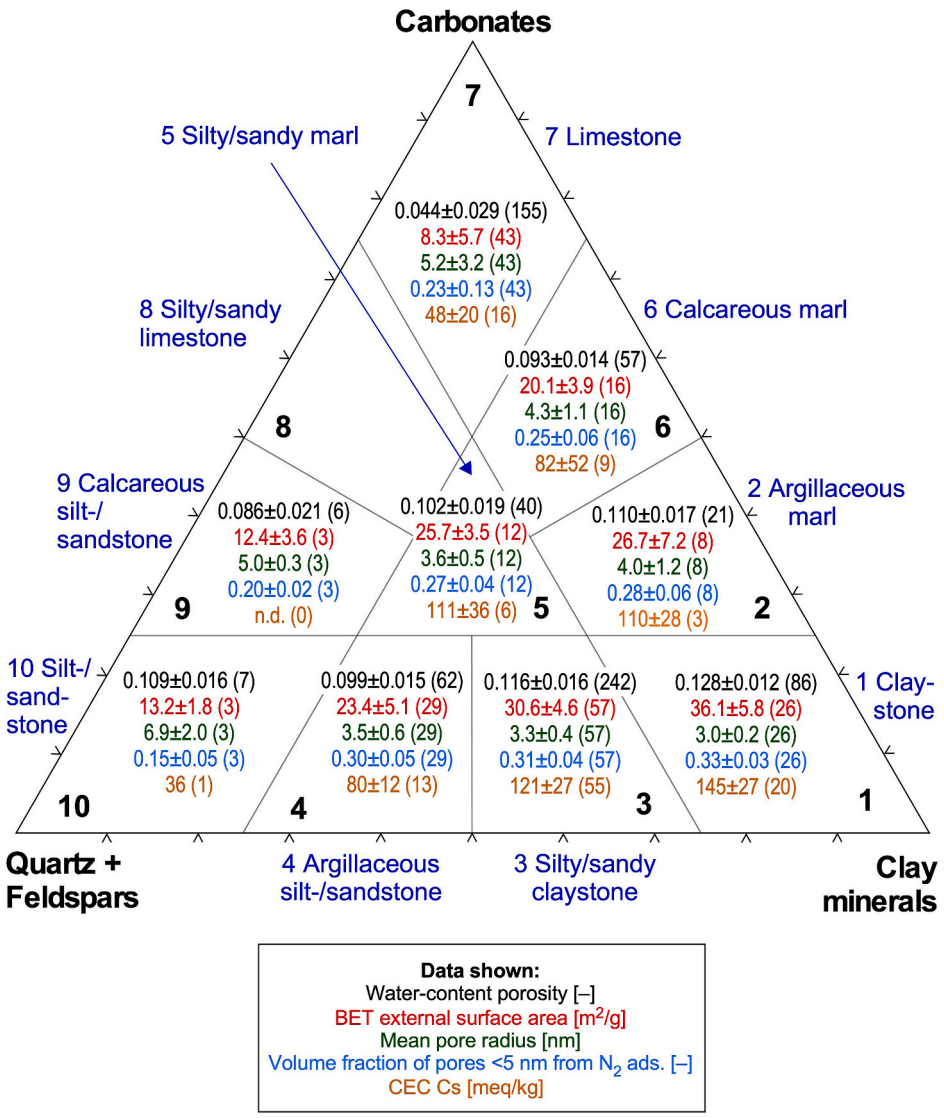

Fig. 6. Key data (average±1σ, number of samples) for Jurassic samples shown in the Füchtbauer triangle (Füchtbauer 1988). Axes are in wt.%. Samples with >10 % minerals other than those represented by the triangle are excluded.

rocks and limestones. In particular, the presence of anhydrite reduces porosity substantially, and values tend towards zero in massive anhydrite beds (Fig. 7b). Thus, anhydrite-rich units in the Triassic may act as barriers to solute transport via the pore space in the vertical dimension, whether by advection or by diffusion.

4.3. *Surface area and pore-size distribution based on N_2 adsorption*

N_2 adsorption-desorption isotherms were acquired for the characterisation of microfabrics. The standard BJH approach (Barrett et al., 1951) provides estimates of pore-size distributions in the range 2–200 nm. Note that pore-size distributions based on NMR cryoporometry, a method that is able to resolve pore apertures up to 1 μm, indicate the absence of pores larger than 200 nm (Fleury et al., 2022). Given the fact that N_2 does not enter interlayers of clay minerals, it characterises only the so-called external porosity. External surface areas were obtained using the BET protocol (Brunauer et al., 1938). Fig. 6 shows that the external surface area is highest in claystones (average 36.1 m^2/g) and decreases systematically towards the carbonate (8.3 m^2/g in limestones) and quartz (13.2 m^2/g in silt/sandstones) corners of the triangle. An excellent correlation is found between clay content and BET surface (Fig. 8a). The same is true for the correlation with porosity (not shown), except for Fe-rich oolites that partially fall off from the general trend. This issue is further addressed in the Discussion section below.

Examples of pore-size spectra for the lithologies represented in the triangle of Fig. 6 are shown in Fig. 8c and d. For the y axis, the quantity $(dV_p/d\ln d_p)/w$ is shown, which means that the area below the curve of any specific range of pore diameters d is proportional to the contribution of this range to the total pore space V. In addition, the spectra are normalised to the water content w, measured by gravimetric water loss, yielding relative size distributions that are directly comparable among samples, independently of porosity. In clay-rich lithologies 1–3 as defined in Fig. 6, the size distribution based on the adsorption branch shows a prominent peak at 2–3 nm, which can be associated with clay minerals, as its amplitude decreases with decreasing clay content (shown in Fig. 8b). In carbonate-rich lithologies 6 and 7 (most of which still contain a small proportion of clay minerals), a broad peak in the range 40–100 nm dominates instead. Bimodal distributions with both peaks at comparable amplitude are found for intermediate lithologies 4, 5 and 9. In silt-/sandstones (lithology 10), a broad plateau over a wide range of pore sizes is found. Thus, pore-size distributions vary systematically between lithologies, and clay-rich lithologies tend to be dominated by the smallest pore diameters in the range of a few nm. Mean radii of external pores can be estimated by dividing the water content

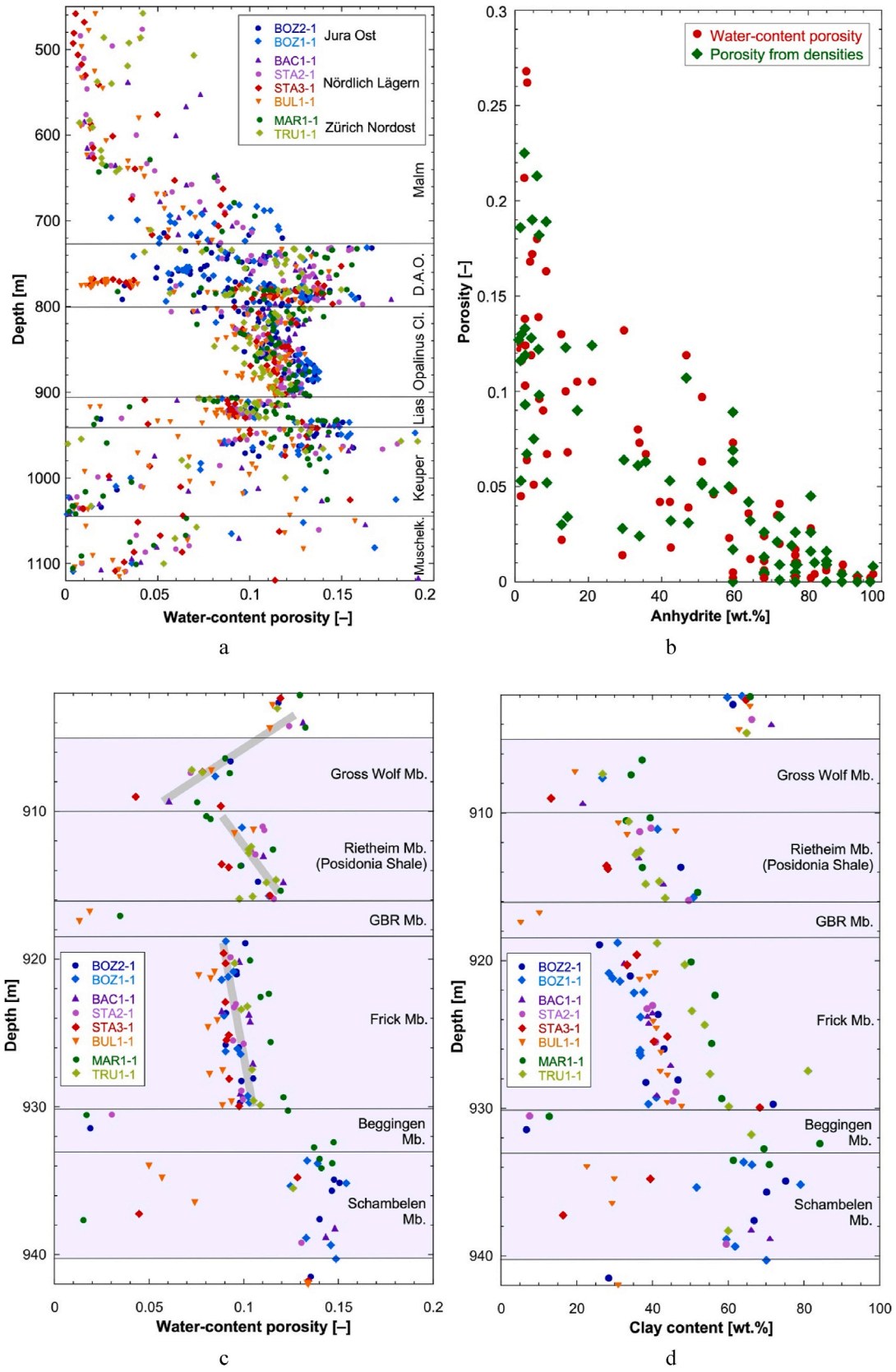

Fig. 7. Porosity as a function of depth and of mineralogical composition. a. Distribution of water-content porosity over the studied profiles. Depth data are adjusted to the profile of the STA2-1 borehole. D.A.O. = Dogger above Opalinus Clay. b. Porosity as a function of anhydrite content in samples from the Triassic. c, d. Profiles of water-content porosity and of clay content over the heterogeneous Lias section (coloured background). Grey bars in c. highlight observed trends. GBR Mb. = Grünschholz, Breitenmatt + Rickenbach Mb. Depth data are adjusted to the profile of the STA2-1 borehole.

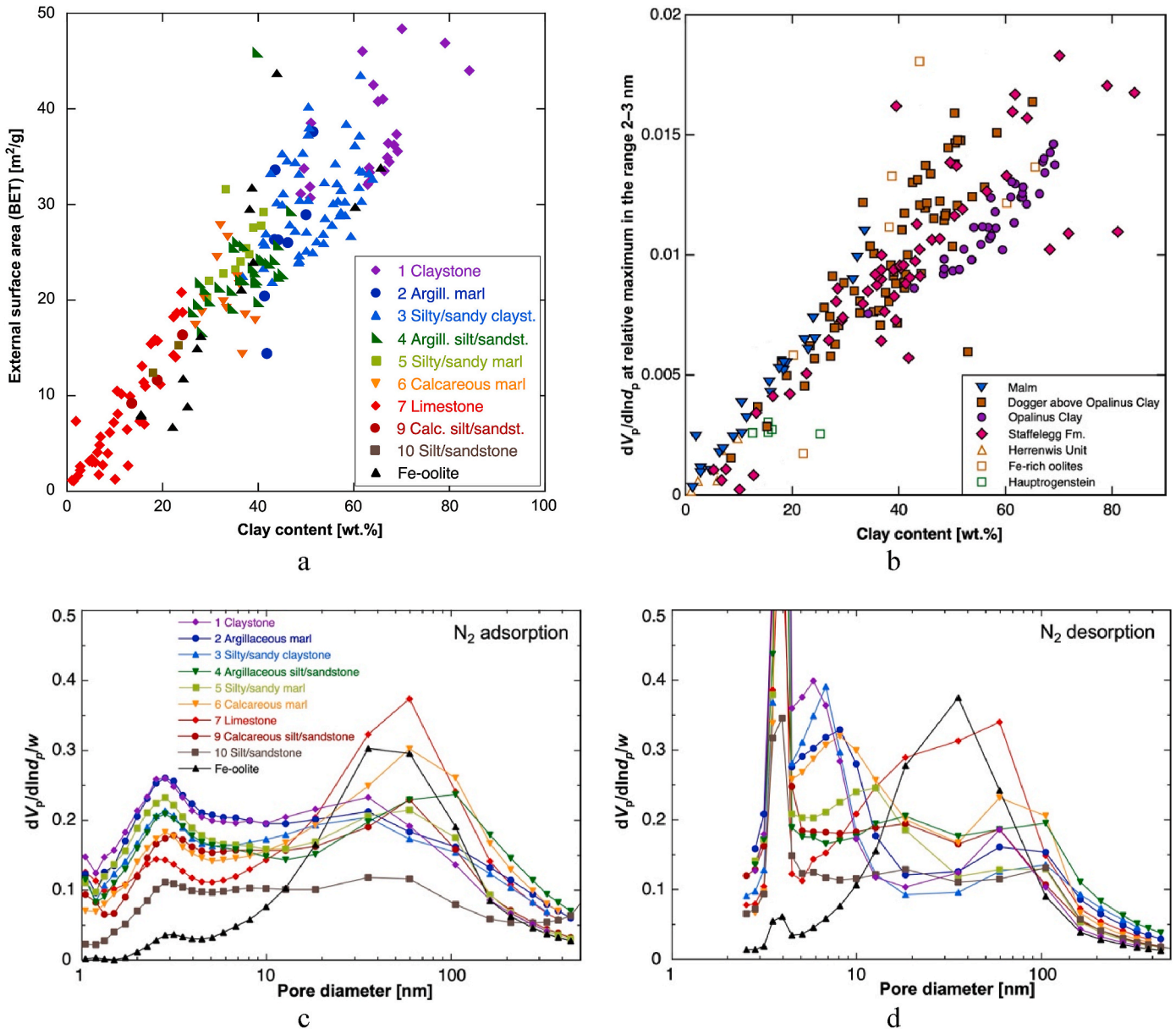

Fig. 8. Results of N_2 ad-/desorption analyses. a: BET surface area as a function of clay content. b: Absolute height of the peak at 2–3 nm in pore-size spectra based on N_2 adsorption as a function of clay content. Open symbols highlight units with special pore-size architectures (see text). c, d: Examples of pore-size distributions based on the N_2 ad- and desorption branches, obtained using the BJH algorithm, normalised to the water content of the samples. 1 = TRU1-1 923.34, Opalinus Clay, Clay-rich sub-unit; 2 = BUL1-1 808.92, Parkinsoni-Württembergica-Schichten; 3 = BUL1-1 965.46, Opalinus Clay, Mixed clay-silt-carbonate sub-unit; 4 = TRU1-1 788.76, Wedelsandstein Fm.; 5 = STA3-1 748.38, Wedelsandstein Fm.; 6 = MAR1-1 717.76, Staffelegg Fm., Rietheim Mb.; 7 = BOZ1-1 323.16, Wildegg Fm., Effingen Mb.; 9 = MAR1-1 588.40, Wedelsandstein Fm.; 10 = TRU1-1 812.24, Wedelsandstein Fm.; Fe-rich oolite BOZ2-1 313.13, Hauptrogenstein, Spatkalk.

relative to dry weight by the BET surface area and the water density. Indeed, as seen in Fig. 6, the mean pore radius is lowest in claystones (3.0 nm) and doubles towards limestones and silt-/sandstones, indicating that the architecture of the pore space changes substantially between different lithologies.

Given the fact that mesoporous materials typically show a hysteresis loop during ad/desorption of N_2 (Thommes et al., 2015), pore-size distributions obtained from desorption look somewhat different (Fig. 8d). This is partly related to connectivity effects or pore blocking, which may be more pronounced during desorption than during adsorption. Accordingly, desorption tests tend to provide information related to pore throat sizes, but other effects (e.g. metastability of liquid or vapour phase, liquid bridges; Thommes et al., 2015) may also contribute to hysteresis. A narrow peak at 4 nm is the most prominent feature in most lithologies. It is attributed to liquid instabilities, i.e. changes of the configuration of liquid nitrogen during desorption, such as the breakage of menisci during progressive desorption, leading to a partial closure of the hysteresis loop. The pore volume associated to the peak at 4 nm is thus associated with pores over a somewhat wider range (Groen et al., 2003; Kuila and Prasad 2013). The height of the peak (and the pore-volume fraction related to this peak) shows a positive correlation with clay content and so is likely related to pores associated with clay minerals. Clay-rich lithologies show a second, broad and less well expressed peak in the range 5–8 nm. Similar to the adsorption isotherms, carbonate-rich lithologies show a broad peak in the range 20–100 nm that is not seen in other lithologies.

5. Discussion

5.1. Pore-size distributions based on N_2 adsorption

The proportionality between the height of the peak at 2–3 nm in adsorption isotherms and the clay content as seen in Fig. 8b suggests that the volume fraction of pores smaller than about 5 nm is characteristic of pore space related to clay minerals. Statistical data pertinent to this volume fraction are shown in Fig. 6. The average value is 0.33 for claystones and decreases towards limestones and silt/sandstones. Note that for all parameters shown in Fig. 6, the relative variability of the data is highest for limestones, meaning that these comprise a range of fabrics, as noted previously by other authors (e.g. Lucia 2007). Thus, mineralogy alone is not the only factor that determines the pore-space distribution.

Nevertheless, even in the most clay-rich samples a substantial pore-volume fraction is related to apertures >5 nm, as seen in Fig. 8 for the claystone sample. Thus, while the fraction of the pore volume related to pore sizes <5 nm is closely related to clay porosity, larger pore apertures are also present. Further, the BJH algorithm to interpret N_2 adsorption in terms of pore sizes is a physical model based on a number of assumptions that do not fully capture the complexity of natural rock fabrics. This also means that the absolute values of the pore sizes are somewhat uncertain, and the obtained spectra may differ from those derived from alternative methods, such as adsorption of H_2O (e.g. Gimmi and Churakov 2019) or NMR cryoporometry (e.g. Fleury et al., 2015, 2022). Finally, samples are dried prior to the acquisition of N_2 ad/desorption isotherms, which leads to the collapse of interlayer porosity in smectite. This volume loss is compensated by the widening of larger pores or the creation of shrinkage microcracks.

Only limited data are available for silty/sandy lithologies, but the pore-size distributions are consistent in that they show a small peak at 2–3 nm in the adsorption isotherms (attributed to clay minerals) and a plateau until about 100 nm. This plateau distinguishes silt/sandstones from calcite-rich lithologies that show a broad peak at 40–100 nm that

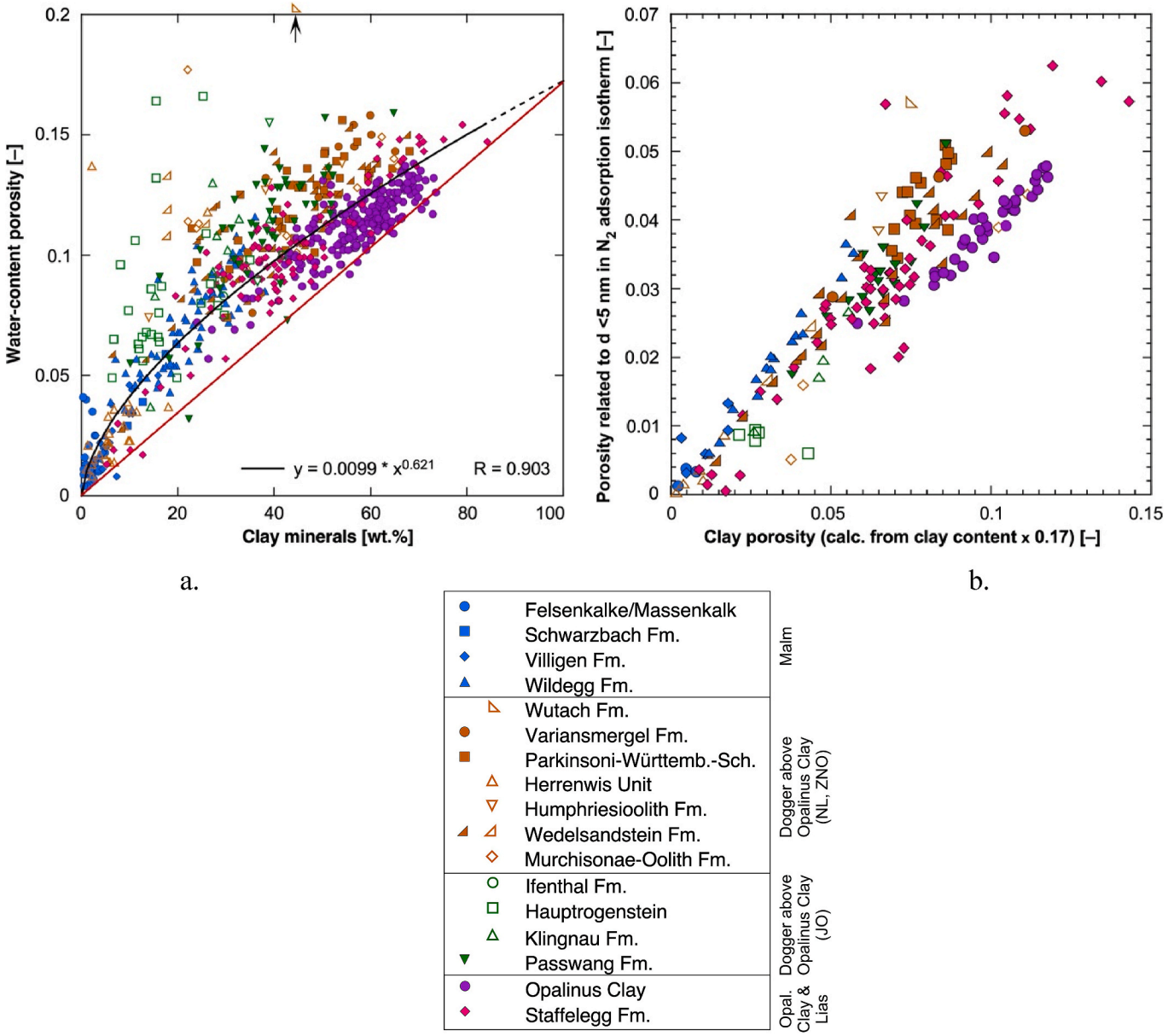

Fig. 9. Relationship between clay content and porosity in the Jurassic section. a. Water-content porosity as a function of clay content. Points with open symbols were not considered for the calculation of the black fit curve (see text). Arrow points to a sample with a porosity of 0.30. b. Correlation between clay porosity calculated from clay content and porosity related to pores <5 nm obtained from N_2 adsorption isotherms.

becomes higher with increasing carbonate content (Fig. 8). The difference between silty/sandy lithologies and limestones may be related to the fact that the grain size of quartz that dominates silt/sandstones is in the silty and sandy fraction, whereas the grain sizes of calcite grains span a much wider range (micrite to macrofossil).

5.2. Relationship between clay content and porosity

Focussing on the Jurassic part of the profile, there is a good correlation between clay content and water-content porosity (Fig. 9a). After excluding several data points (shown by open symbols in Fig. 9a; justification follows below), a power-law function well fits the measured data. The slope of the fit curve is 0.010–0.016 at low clay contents but flattens out to <0.0015 at contents >40 wt%. In order to explain the changing slope, the pore-size distributions obtained from N_2 adsorption (Fig. 8) need to be considered. In these, two peaks can be distinguished, one with a mode at 2–3 nm, the other at 40–100 nm. As stated above, the 2–3 nm peak is characteristic of clay minerals, most likely to porosity related to the stacking of clay aggregates, and it is absent in pure limestones. The peak (or plateau) in the range 40–100 nm can be observed in all samples but becomes, in relative terms, more prominent with increasing calcite content (Fig. 8). The pores in this size range are attributed to the mingling of grains of different sizes and shapes in the rock matrix, namely of platy clay minerals and granular, essentially isometric calcite. Geometric incompatibilities related to the different grain shapes (and also the distinct behaviour during mechanical compaction) are suggested as the likely reason for the presence of larger pores in clay-carbonate mixtures. Indeed, such incompatibilities have been imaged in various TEM and STEM studies of shales (e.g. Curtis et al., 2012, Keller et al., 2013a). The concept considering these two types of pores is illustrated in Fig. 10.

Taking this idea further, the porosity data as shown in Fig. 9a can be considered to consist of two contributions: 1) *Clay porosity* between clay aggregates, with sizes of a few nm, and 2) *porosity related to geometric incompatibilities* between platy and granular minerals, with sizes in the range of tens of nm. Clay porosity can be assumed to be proportional to the clay content, whereas porosity due to incompatibilities is present in clay-carbonate mixtures but not in pure clay or carbonate. Extrapolating the trend line fitting the measured data in Fig. 9a to pure clay leads to a porosity of 0.17. The red line then reflects the clay porosity, considering proportionality with the clay content. The curvature in the fit line reflects the additional pore type that occurs in lithologies in which platy clay minerals occur together with more isometric grains of calcite. The contribution of this pore type is at a maximum when both mineral types occur in comparable proportions and is of lesser relevance towards the pure clay and non-clay compositions. The clay porosity calculated by assuming proportionality with the clay content shows an excellent correlation with the porosity related to pore diameters <5 nm as derived from N_2 adsorption data (Fig. 9b). This correlation is better than when considering the measured water-content porosity on the x-axis (not shown), confirming that the peak at 2–3 nm is indeed related to clay porosity.

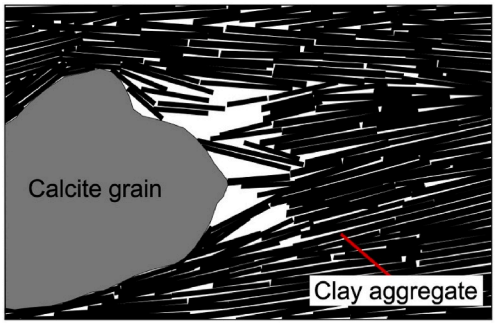

Fig. 10. Conceptual view of the porosity types (white) in clay-carbonate mixtures, inspired by a STEM image by Curtis et al. (2012). Width of field is ~1 μm.

It can also be seen in Fig. 9 that even at the same clay content, systematic differences of porosity exist between different geological units. For example, the Opalinus Clay has a lower porosity than the overlying Dogger units of comparable clay content, a finding that cannot be explained by the only marginally different maximum burial depths. Rock fabric and porosity thus depend on other parameters as well, such as the rate of sediment deposition because it is related to the time available for early diagenesis. A low deposition rate means that the time period over which early diagenesis acted on the unconsolidated sediment was longer, potentially leading to more extensive mineral reactions, such as dissolution and cementation, with consequences for the rock fabric and its behaviour during later compaction. Data pertinent to deposition rates were provided by Wohlwend et al. (2021a,b, 2022) based on ammonite stratigraphy and palynological analysis. The Opalinus Clay was deposited at a rate of about 50–60 m/Myr (referring to the current thickness in the compacted state), which is more than for any of the other Dogger units. The rapid burial is consistent with the observation that the Opalinus Clay is only weakly cemented and disaggregates when immersed in pure water, except in silty lenses in which sparitic calcite fills the pore space. In comparison, the average deposition rates for the underlying Staffelegg Fm. and the Dogger above Opalinus Clay (D.A.O.) were 1.3–1.6 and 10–14 m/Myr, respectively, thus leaving more time for early diagenetic cementation and leading to a stiffer behaviour during compaction.

It is noteworthy that, with a few exceptions, porosity of clay-poor lithologies tends towards 0 (Fig. 9a). This is an evident difference to the theoretical model developed by Revil and Cathles (1999) for the relationship between clay content, porosity and permeability in sand-clay mixtures. In this model, the addition of a clay component to a sandstone resulted in a reduction of porosity because the clay fills the intergranular pore space between the large grains. A porosity minimum is reached when the volumetric clay content was identical to the porosity of the pure sandstone, at which point all large pores are filled with clay. A further increase of clay content implies a lower proportion of sand grains, thus porosity increases until reaching the value of the pure claystone. This geometrical model appears to be at odds with the data shown in Fig. 9a where porosity increases steadily with clay content. However, this can be explained by the fact that the data shown here essentially refer to carbonate-(sand-)clay mixtures, whereas Revil and Cathles (1999) considered pure sand-clay mixtures. The latter are characterised by a bimodal grain-size distribution of large sand grains and much smaller clay minerals. In contrast to the generally well sorted sand component, carbonate minerals in the rocks studied here occur over a wide range of grain sizes (macrofossils to micrite), and there is no strictly bimodal grain-size distribution that was assumed by Revil and Cathles (1999). Moreover, these authors did not consider chemical effects, such as pressure solution and cementation, while these are of importance in our case.

More recently, Bourg (2015) presented a worldwide review of measured data pertinent to the dependence of porosity on clay content. In the range 0–30 wt% clay, porosity was found to increase only marginally with clay content and remained around 0.05 even for clay-free lithologies. The slope increased strongly at clay contents >30 wt%, which was explained by the transition from a grain-supported to a matrix-supported fabric. The study suggests a convex trend, while the data in Fig. 9a define a concave curve. However, there are some differences and issues:

- The data for formations with clay contents <30 wt% shown by Bourg (2015) are dominated by North American gas shales, which are mostly silt/sandstones in the nomenclature of Füchtbauer (1988), while the clay-poor units in this study are predominantly limestones and calcareous marls, i.e. quartz-poor lithologies.

- The correlation of Bourg (2015) combines data of formations that underwent a wide range of maximum burial depths. The North American gas shales with lower clay contents were typically buried to depths of several kilometres (e.g. Jarvie et al., 2007; Curtis et al., 2012) and so are highly compacted and over-consolidated at their current depths. On the other hand, the data pertinent to formations with clay contents >30 wt% comprise data from highly consolidated units (such as the Haynesville Shale, maximum burial depth ≥3 km; Nunn 2012; Dowey and Taylor 2020), from intermediate levels (such as the Opalinus Clay, 1.7 km; Mazurek et al., 2006) and units that were subjected to shallow burial only (such as the Boom Clay, 0.2 km; Vandenberghe et al., 2014). The wide spread of the data (and the absence of a correlation) is related to the fact that porosity is not only a function of clay content but also of the degree of compaction and over-consolidation. Note that the data in the present study refer to a narrow depth range.

Overall, it can be concluded that clay content is not the only mineralogical parameter that governs petrophysical rock properties, and that the nature of the non-clay fraction also matters, with evident differences between clay-carbonate and clay-sand mixtures. The properties of clastic-calcareous sedimentary rocks are best explored by considering the mineralogical composition in a ternary system, as shown in Fig. 6.

A number of outliers towards higher porosity can be identified in Fig. 9. They originate from Fe-rich oolites (e.g. Wutach Fm., Humphriesioolith-Fm., Murchisonae-Oolith Fm.), from the Hauptrogenstein (oolitic limestone) and from the reef facies of the Herrenwis Unit. All samples from these units are shown with open symbols, together with sandstones (but not the more clay-rich lithologies) of the Wedelsandstein Fm. All these units have in common that at the time of deposition, they contained large mechanically competent grains, such as ooids, abundant quartz in the sand fraction and coarse-grained calcite from the reef. It is conceivable that the compaction of such grain-supported lithologies led to less reduction of porosity when compared with the other, in general matrix-supported units (clay and micrite).

Another mechanism that counteracts compaction is cementation during early diagenesis. Several (but not all) of the studied Fe-rich oolites are condensed horizons reflecting a low deposition rate, thus leaving long periods of time for early diagenetic cementation that leads to more competent fabrics that behave differently during compaction than other lithologies of comparable composition. The sample with the highest measured porosity of 0.3 originates from the Wutach Fm., a Fe-rich oolite at the top of the Dogger. The deposition rate, derived for boreholes BUL1-1 and MAR1-1 by Wohlwend et al. (2021a,b), is in the range 1.3–1.5 m/Myr – thus, the deposition of only 1.2–3 m of sediment (thickness measured in its current state) took 0.9–2 Myr, a time period comparable to that needed to deposit 100–120 m of Opalinus Clay.

A representative example of the pore-size distribution of an Fe-rich oolite is shown in Fig. 8. In spite of a clay content of 25 wt%, the peak at 2–3 nm is almost absent, and the largest fraction of the pores is related to apertures of tens of nm. With a range of 6–20 nm, Fe-rich oolites have the largest mean pore diameters of all lithologies, and this also explains the high anion accessibility of the pore space that is typical for these rocks (Zwahlen et al., 2023).

6. Conclusions

In study areas Nördlich Lägern and Zürich Nordost, the low-permeability sequence has a thickness of 400 m or more and is bounded by the regional Malm aquifer in the hanging wall and by the regional Muschelkalk or the local Keuper aquifer in the footwall. In the Jura Ost area, its thickness is about 300 m, with the Hauptrogenstein at the upper and the Keuper aquifer at the lower boundary. It consists of clay-rich and carbonate-rich units, with less frequent sandy lithologies. Anhydrite-rich units separate the Keuper and Muschelkalk aquifers and, given their low porosity, act as barriers to mass transport in the vertical dimension. The Opalinus Clay in the centre of the low-permeability sequence is the most homogeneous unit in both the vertical and horizontal dimensions.

Rock porosity and pore-size distribution depend on the mineralogical composition, in particular on the clay content. However, formation-specific differences are evident even at comparable clay contents and are attributed to different extents to which early diagenesis affected the sediment close to the seafloor, which in turn is a function of the deposition rate, which varied widely during the Jurassic. The degree of early diagenetic cementation is low in the Opalinus Clay, most probably due to its rapid deposition.

The relationship between clay content and porosity shows a curved profile with a flattening slope at high clay contents. Together with the pore-size distributions obtained from N_2 adsorption, two pore types were distinguished: 1) Nanometric pores related to the stacking of clay aggregates, resulting in a porosity proportional to the clay content, and 2) pores in the size range 40–100 nm that are related to the mingling of clay minerals with larger, stiffer grains, resulting in geometric incompatibilities and a distinct compaction behaviour. As the latter pore type only occurs in mixtures of clay minerals and larger grains and is not present in the pure endmembers, it accounts for the curvature of the clay content-porosity curve.

Rock units that contained larger mineral grains at the time of deposition (such as oolites, sandstones and reef limestone) show a distinct behaviour during compaction. The presence of large competent grains, resulting in local pressure shadows or a grain-supported fabric, limited the degree of compaction, leading to higher porosities and average pore apertures than in other rocks of comparable mineralogical composition. Fe-rich oolites, typically related to low deposition rates, are most strongly affected by early diagenetic effects, such as mineral dissolution and cementation. They show distinct pore-size distributions with a predominance of pore diameters in the range of tens of nm but only a small contribution of nanopores that are typical of clay-bearing lithologies.

Porosity of clay-quartz mixtures depends only weakly on the clay/quartz ratio, which is attributed to the development of a grain-supported fabric in sandy lithologies. In contrast, porosity decreases substantially with increasing carbonate content in clay/carbonate mixtures and tends towards quite low values in pure limestone, likely due to pressure solution and partial recrystallisation.

Declaration of competing interest

The authors declare that they have no known competing financial interests or personal relationships that could have appeared to influence the work reported in this paper.

Data availability

Data will be made available on request.

Acknowledgements

The authors thank Nagra (National Cooperative for the Disposal of Radioactive Waste, Wettingen, Switzerland) for financial support. Thoughtful comments by Dr Q. Fisher (Uni. Leeds, UK) and an anonymous reviewer are gratefully acknowledged. All authors who contributed to the Special Issue would like to thank the guest editors Dr Adrian Bath (Intellisci, UK), Dr Mieke De Craen (SCK-CEN, Belgium) and Dr Erika A.C. Neeft (Covra, Netherlands) for their great commitment, as well as the proactive support of the Editor-in-Chief Dr Zimeng Wang (Fudan University, Shanghai, China).

Appendix A. Supplementary data

Supplementary data to this article can be found online at https://doi.org/10.1016/j.apgeochem.2023.105839.

References

Aschwanden, L., Diamond, L.W., Mazurek, M., Davis, D.W., 2019a. Creation of secondary porosity in dolostones by upwelling basement water in the foreland of the Alpine orogen. Geofluids 2019. https://doi.org/10.1155/2019/5210404.

Aschwanden, L., Diamond, L.W., Adams, A., 2019b. Effects of progressive burial on matrix porosity and permeability of dolostones in the foreland basin of the Alpine Orogen, Switzerland. Mar. Petrol. Geol. 100, 148–164. https://doi.org/10.1016/j.marpetgeo.2018.10.055.

Aschwanden, L., Camesi, L., Gimmi, T., Jenni, A., Kiczka, M., Mäder, U., Mazurek, M., Rufer, D., Waber, H.N., Wersin, P., Zwahlen, C., Traber, D., 2021. TBO Trüllikon-1-1 – Data report, Dossier VIII: Rock properties, porewater characterisation and natural tracer profiles. Nagra Arbeitsbericht NAB 20-09, Nagra, Wettingen, Switzerland. Available at nagra.ch.

Aschwanden, L., Camesi, L., Gaucher, E., Gimmi, T., Jenni, A., Kiczka, M., Mäder, U., Mazurek, M., Rufer, D., Waber, H.N., Wersin, P., Zwahlen, C., Traber, D., 2022. TBO Stadel 3-1 – Data report, Dossier VIII: Rock properties, porewater characterisation and natural tracer profiles. Nagra Arbeitsbericht NAB 22-01, Nagra, Wettingen, Switzerland. Available at nagra.ch.

Aschwanden, L., Waber, H.N., Eichinger, F., Gimmi, T., 2023a. Isotope diffusive exchange experiments for deriving porewater isotope composition in low-permeability rocks – Improvements in experimental procedure and data processing. Appl. Geochem. 105844 https://doi.org/10.1016/j.apgeochem.2023.105844.

Aschwanden, L., Wersin, P., Debure, M., Traber, D., 2023b. Experimental study of water-extractable sulphate in Opalinus Clay and implications for deriving porewater concentrations. Appl. Geochem. 105837 https://doi.org/10.1016/j.apgeochem.2023.105837.

Barrett, E.P., Joyner, L.G., Halenda, P.P., 1951. The determination of pore volume and area distributions in porous substances. I. Computations from nitrogen isotherms. J. Am. Chem. Soc. 73, 373–380.

Becker, A., 2000. The Jura Mountains—an active foreland fold-and thrust belt? Tectonophysics 321, 381–406.

Bensenouci, F., Michelot, J.L., Matray, J.M., Savoye, S., Lavielle, B., Thomas, B., Dick, P., 2011. A profile of helium-4 concentration in pore-water for assessing the transport phenomena through an argillaceous formation (Tournemire, France). Phys. Chem. Earth 36, 1521–1530. https://doi.org/10.1016/j.pce.2011.10.016.

Bensenouci, F., Michelot, J.L., Matray, J.M., Savoye, S., Tremosa, J., Gaboreau, S., 2013. Profiles of chloride and stable isotopes in pore-water obtained from a 2000 m-deep borehole through the Mesozoic sedimentary series in the eastern Paris Basin. Phys. Chem. Earth 65, 1–13. https://doi.org/10.1016/j.pce.2011.10.024.

Bensenouci, F., Michelot, J.L., Matray, J.M., Savoye, S., Massault, M., Vinsot, A., 2014. Coupled study of water-stable isotopes and anions in porewater for characterizing aqueous transport through the Mesozoic sedimentary series in the eastern Paris Basin. Mar. Petrol. Geol. 53, 88–101. https://doi.org/10.1016/j.marpetgeo.2013.12.012.

BFE, 2018. Sachplan geologische Tiefenlager: Ergebnisbericht zu Etappe 2: Festlegungen und Objektblätter. Bundesamt für Energie BFE (Swiss Federal Office of Energy), Bern, Switzerland. Available at. www.bfe.admin.ch.

Bourg, I.C., 2015. Sealing shales versus brittle shales: a sharp threshold in the material properties and energy technology uses of fine-grained sedimentary rocks. Environ. Sci. Technol. Lett. 2015, 255–259. https://doi.org/10.1021/acs.estlett.5b00233.

Brunauer, S., Emmett, P.H., Teller, E., 1938. Adsorption of gases in multimolecular layers. J. Am. Chem. Soc. 60, 309–319. https://doi.org/10.1021/ja01269a023.

Clark, I.D., Al, T., Jensen, M., Kennell, L., Mazurek, M., Mohapatra, R., Raven, K.G., 2013. Paleozoic-aged brine and authigenic helium preserved in an Ordovician shale aquiclude. Geology. https://doi.org/10.1130/G34372.1.

Curtis, M.E., Ambrose, R.J., Sondergeld, C.H., Rai, C.S., 2011. Transmission and scanning electron microscopy investigation of pore connectivity of gas shales on the nanoscale. Soc. Petrol. Eng., SPE, 144391.

Curtis, M.E., Sondergeld, C.H., Ambrose, R.J., Rai, C.S., 2012. Microstructural investigation of gas shales in two and three dimensions using nanometer-scale resolution imaging. AAPG Bull. 96, 665–677.

Dowey, P.J., Taylor, K.G., 2020. Diagenetic mineral development within the upper Jurassic Haynesville-Bossier shale, USA. Sedimentology 67, 47–77.

Egli, D., Mosar, J., Ibele, T., Madritsch, H., 2016. The role of precursory structures on Tertiary deformation in the Black Forest—Hegau region. Int. J. Earth Sci. https://doi.org/10.1007/s00531-016-1427-8.

Fleury, M., Fabre, R., Webber, J.B.W., 2015. Comparison of pore size distribution by NMR relaxation and NMR cryoporometry in shales. Intern. Symp. Soc. Core Anal., SCA 25, 25–36.

Fleury, M., Gimmi, T., Mazurek, M., 2022. Porewater content, pore structure and water mobility in clays and shales from NMR methods. Clays Clay Miner. https://doi.org/10.1007/s42860-022-00195-4.

Füchtbauer, H., 1988. Sedimente und Sedimentgesteine. E. Schweizerbart'sche Verlagsbuchhandlung, Stuttgart, Germany.

Gaucher, E., Aschwanden, L., Camesi, L., Gimmi, T., Jenni, A., Kiczka, M., Mäder, U., Mazurek, M., Rufer, D., Waber, H.N., Wersin, P., Zwahlen, C., Traber, D., 2023. TBO Bachs 1-1 – Data report, Dossier VIII: Rock properties, porewater characterisation and natural tracer profiles. Nagra Arbeitsbericht NAB 22-04, Nagra, Wettingen, Switzerland. Available at nagra.ch.

Gimmi, T., Churakov, S.V., 2019. Water retention and diffusion in unsaturated clays: connecting atomistic and pore scale simulations. Appl. Clay Sci. 175, 169–183. https://doi.org/10.1016/j.clay.2019.03.035.

Gimmi, T., Waber, H.N., Gautschi, A., Rübel, A., 2007. Stable water isotopes in pore water of Jurassic argillaceous rocks as tracers for solute transport over large spatial and temporal scales. Water Resour. Res. 43, W04410 https://doi.org/10.1029/2005WR004774.

Gimmi, T., Aschwanden, L., Camesi, L., Gaucher, E., Jenni, A., Kiczka, M., Mäder, U., Mazurek, M., Rufer, D., Waber, H.N., Wersin, P., Zwahlen, C., Traber, D., 2022. TBO Bözberg-2-1 – Data report, Dossier VIII: Rock properties, porewater characterisation and natural tracer profiles. Nagra Arbeitsbericht NAB 21-22, Nagra, Wettingen, Switzerland. Available at nagra.ch.

Gimmi, T., Aschwanden, L., Waber, H.N., Gaucher, E.C., Ma, J., Traber, D., 2023. Profiles of $\delta^{18}O$ and $\delta^{2}H$ in porewater of a Mesozoic rock sequence: Regional variability and relation to large-scale transport regimes. Appl. Geochem., 105846. https://doi.org/10.1016/j.apgeochem.2023.105846.

Glaus, M.A., Van Loon, L.R., Wüst, R.A.J., 2023. Diffusion of HTO, $^{36}Cl^{-}$ and $^{22}Na^{+}$ in the Mesozoic rocks of Northern Switzerland. II: Data interpretation in terms of an electrical double layer model. Appl. Geochem., 105842. https://doi.org/10.1016/j.apgeochem.2023.105842.

Groen, J.C., Peffer, L.A.A., Pérez-Ramírez, J., 2003. Pore size determination in modified micro- and mesoporous materials. Pitfalls and limitations in gas adsorption data analysis. Microporous Mesoporous Mater. 60, 1–17.

Houben, M.E., Desbois, G., Urai, J.L., 2013. Pore morphology and distribution in the Shaly facies of Opalinus Clay (Mont Terri, Switzerland): insights from representative 2D BIB–SEM investigations on mm to nm scale. Appl. Clay Sci. 71, 82–97.

Houben, M.E., Desbois, G., Urai, J.L., 2014. A comparative study of representative 2D microstructures in Shaly and Sandy facies of Opalinus Clay (Mont Terri, Switzerland) inferred from BIB-SEM and MIP methods. Mar. Petrol. Geol. 49, 143–161.

Iannotta, J., Eichinger, F., Traber, D., 2023. TBO Rheinau-1-1 – Data report, Dossier VIII: Profile of stable isotopes in porewater. Nagra Arbeitsbericht NAB 22-03, Nagra, Wettingen, Switzerland. Available at nagra.ch.

Jarvie, D.M., Hill, R.J., Ruble, T.E., Pollastro, R.M., 2007. Unconventional shale-gas systems: the Mississippian Barnett Shale of north-central Texas as one model for thermogenic shale-gas assessment. AAPG Bull. 91, 475–499.

Keller, L.M., Holzer, L., Wepf, R., Gasser, P., Münch, B., Marschall, P., 2011. On the application of focused ion beam nanotomography in characterizing the 3D pore space geometry of Opalinus clay. Phys. Chem. Earth 36, 1539–1544.

Keller, L.M., Schuetz, P., Erni, R., Rossell, M., Lucas, F., Gasser, P., Holzer, L., 2013. Characterization of multi-scale microstructural features in Opalinus Clay. Microporous Mesoporous Mater. 170, 83–94. https://doi.org/10.1016/j.micromeso.2012.11.029.

Kiczka, M., Wersin, P., Mazurek, M., Zwahlen, C., Jenni, A., Mäder, U., Traber, D., 2023. Porewater composition in clay rocks explored by advective displacement and squeezing experiments. Appl. Geochem., 105838. https://doi.org/10.1016/j.apgeochem.2023.105838.

Klaver, J., Hemes, S., Houben, M., Desbois, G., Radi, Z., Urai, J.L., 2015. The connectivity of pore space in mudstones: insights from high-pressure Wood's metal injection, BIB-SEM imaging, and mercury intrusion porosimetry. Geofluids. https://doi.org/10.1111/gfl.12128.

Kuila, U., Prasad, M., 2013. Specific surface area and pore-size distribution in clays and shales. Geophys. Prospect. 61, 341–362.

Laubscher, H., 1972. Some overall aspects of Jura dynamics. Am. J. Sci. 272, 293–304.

Lerouge, C., Grangeon, S., Claret, F., Gaucher, E., Blanc, P., Guerrot, C., Flehoc, C., Wille, G., Mazurek, M., 2014. Mineralogical and isotopic record of diagenesis from the Opalinus Clay formation at Benken, Switzerland: implications for the modeling of pore-water chemistry in a clay formation. Clays Clay Miner. 62, 286–312.

Lucia, F.J., 2007. Carbonate Reservoir Characterization, 2nd Edition. Springer, Berlin, p. 336.

Mäder, U., 2018. Advective displacement method for the characterisation of pore water chemistry and transport properties in claystone. Geofluids. https://doi.org/10.1155/2018/8198762.

Mäder, U., Aschwanden, L., Camesi, L., Gimmi, T., Jenni, A., Kiczka, M., Mazurek, M., Rufer, D., Waber, H.N., Wersin, P., Zwahlen, C., Traber, D., 2021. TBO Marthalen-1-1 – Data report, Dossier VIII: Rock properties, porewater characterisation and natural tracer profiles. Nagra Arbeitsbericht NAB 21-20, Nagra, Wettingen, Switzerland. Available at nagra.ch.

Madritsch, H., 2015. Outcrop-scale fracture systems in the Alpine foreland of central northern Switzerland: kinematics and tectonic context. Swiss J. Geosci. https://doi.org/10.1007/s00015-015-0203-2.

Malz, A., Madritsch, H., Jordan, P., Meier, B., Kley, J., 2019. Along-strike variations in thin-skinned thrusting style controlled by pre-existing basement structure in the easternmost Jura Mountains (Northern Switzerland). In: Hammerstein, J.A., Di Cuia, R., Cottam, M.A., Zamora, G., Butler, R.W.H. (Eds.), Fold and Thrust Belts: Structural Style, Evolution and Exploration, vol. 490. Geol. Soc. London, Spec. Publ. https://doi.org/10.1144/SP490-2019-090.

Marques Fernandes, M., Mazurek, M., Wersin, P., Wüst, R., Baeyens, B., 2023. Cation-exchange properties of the Mesozoic sedimentary sequence of Northern Switzerland and modelling of the Opalinus Clay porewater. Appl. Geochem., 105852. https://doi.org/10.1016/j.apgeochem.2023.105852.

Mazurek, M., Hurford, A.J., Leu, W., 2006. Unravelling themulti-stage burial history of the Swiss Molasse Basin: integration of apatite fission track, vitrinite reflectance and biomarker isomerisation analysis. Basin Res. 18, 27–50.

Mazurek, M., Alt-Epping, P., Bath, A., Gimmi, T., Waber, H.N., 2009. Natural tracer profiles across argillaceous formations: the CLAYTRAC Project. OECD/NEA report 6253, OECD Nuclear Energy Agency, Paris, France, p. 358. Available at. www.oecdbookshop.org.

Mazurek, M., Alt-Epping, P., Bath, A., Gimmi, T., Waber, H.N., Buschaert, S., De Cannière, P., De Craen, M., Gautschi, A., Savoye, S., Vinsot, A., Wemaere, I., Wouters, L., 2011. Natural tracer profiles across argillaceous formations. Appl. Geochem. 26, 1035–1064.

Mazurek, M., Waber, H.N., Mäder, U.K., Gimmi, T., de Haller, A., Koroleva, M., 2012. Geochemical synthesis for the Effingen Member in boreholes at Oftringen, Gösgen and Küttigen. Nagra Technical Report NTB 12-07, Nagra, Wettingen, Switzerland. Available at nagra.ch.

Mazurek, M., Oyama, T., Wersin, P., Alt-Epping, P., 2015. Pore-water squeezing from indurated shales. Chem. Geol. 400, 106–121.

Mazurek, M., Aschwanden, L., Camesi, L., Gimmi, T., Jenni, A., Kiczka, M., Mäder, U., Rufer, D., Waber, H.N., Wanner, P., Wersin, P., Traber, D., 2021. TBO Bülach-1-1 – Data report, Dossier VIII: Rock properties, porewater characterisation and natural tracer profiles. Nagra Arbeitsbericht NAB 20-08, Nagra, Wettingen, Switzerland. Available at nagra.ch.

Nagra, 2008. Vorschlag geologischer Standortgebiete für das SMA- und das HAA-Lager. Darlegung der Anforderungen, des Vorgehens und der Ergebnisse. Nagra Technical Report NTB 08-03, Nagra, Wettingen, Switzerland. Available at. www.nagra.ch.

NEA, 2009. Considering timescales in the post-closure safety of geological disposal of radioactive waste. NEA No. 6424. Nuclear Energy Agency, Paris, France. Available at. www.oecdbookshop.org.

Nunn, J.A., 2012. Burial and thermal history of the Haynesville Shale: implications for overpressure, gas generation, and natural hydrofracture. Gulf Coast Assoc. Geol. Soc. J. 1, 81–96.

Patriarche, D., Michelot, J.L., Ledoux, E., Savoye, S., 2004a. Diffusion as the main process for mass transport in very low water content argillites: 1. Chloride as a natural tracer for mass transport – diffusion coefficient and concentration measurements in interstitial water. Water Resour. Res. 40, W01516 https://doi.org/10.1029/2003WR002600.

Patriarche, D., Ledoux, E., Michelot, J.L., Simon-Coinçon, R., Savoye, S., 2004b. Diffusion as the main process for mass transport in very low water content argilites: 2. Fluid flow and mass transport modeling. Water Resour. Res. 40, W01517 https://doi.org/10.1029/2003WR002700.

Pearson, F.J., 1999. What is the porosity of a mudrock?. In: Aplin, A., Fleet, A.J., Macquaker, J.H.S. (Eds.), Muds and Mudstones: Physical and Fluid Flow Properties, vol. 158. Geol. Soc. London Spec. Publ, pp. 9–21.

Pearson, F.J., Arcos, D., Bath, A., Boisson, J.Y., Fernandez, A.M., Gäbler, H.E., Gaucher, E., Gautschi, A., Griffault, L., Hernan, P., Waber, H.N., 2003. Mont Terri project – geochemistry of water in the Opalinus Clay formation at the Mont Terri rock laboratory. Federal Office for Water and Geology Report 5, Bern, Switzerland. Available at. www.mont-terri.ch.

Revil, A., Cathles III, L.M., 1999. Permeability of shaly sands. Water Resour. Res. 35, 651–662.

Ring, U., Gerdes, A., 2016. Kinematics of the Alpenrhein-Bodensee graben system in the Central Alps: Oligocene/Miocene transtension due to formation of the Western Alps arc. Tectonics 35, 1367–1391. https://doi.org/10.1002/2015TC004085.

Rogge, T., 1997. Eine molekular-diffusive Methode zur Bestimmung des Porenwassergehaltes und der Zusammensetzung von stabilen Isotopen im Porenwasser von Gestein. Unpubl. Diploma Thesis. Institut für Umweltphysik, University of Heidelberg, Germany.

Rübel, A.P., Sonntag, C., Lippmann, J., Pearson, F.J., Gautschi, A., 2002. Solute transport in formations of very low permeability: profiles of stable isotope and dissolved noble gas contents of pore water in the Opalinus Clay, Mont Terri, Switzerland. Geochim. Cosmochim. Acta 66, 1311–1321.

Rufer, D., Stockhecke, M., 2021. Field manual: Drill core sampling for analytical purposes. Nagra Arbeitsbericht NAB 19-03, Nagra, Wettingen, Switzerland. Available at nagra.ch.

Rufer, D., Waber, H.N., Traber, D., 2023. Vertical and lateral distribution of helium in porewater of the Mesozoic sedimentary sequence of northern Switzerland – A comparative investigation across multiple boreholes. Appl. Geochem., 105836, 2023.105836. https://doi.org/10.1016/j.apgeochem.

RWI, 2020. SGT-E3 Deep Drilling Campaign (TBO): Experiment procedures and analytical methods at RWI. University of Bern (Rock-Water Interaction Group; Version 1.0, April 2020). Nagra Arbeitsbericht NAB 20-13, Nagra, Wettingen, Switzerland. Available at nagra.ch.

Schwarz, R., Schlickenrieder, L., Vogt, T., 2021a. TBO Bülach-1-1: Data Report, Dossier VII: Hydraulic Packer Testing. Nagra Arbeitsbericht NAB 20-08, Nagra, Wettingen, Switzerland. Available at nagra.ch.

Schwarz, R., Schlickenrieder, L., Müller, H.R., Köhler, S., Pechstein, A., Vogt, T., 2021b. TBO Trüllikon-1-1: Data Report, Dossier VII: Hydraulic Packer Testing. Nagra Arbeitsbericht NAB 20-09, Nagra, Wettingen, Switzerland. Available at nagra.ch.

Schwarz, R., Hardie, S.M.L., Müller, H.R., Köhler, S., Pechstein, A., 2021c. TBO Marthalen-1-1: Data Report, Dossier VII: Hydraulic Packer Testing. Nagra Arbeitsbericht NAB 21-20, Nagra, Wettingen, Switzerland. Available at nagra.ch.

Schwarz, R., Beauheim, R., Hardie, S.M.L., Voss, M., Pechstein, A., 2022a. TBO Bözberg-1-1: Data Report, Dossier VII: Hydraulic Packer Testing. Nagra Arbeitsbericht NAB 21-21, Nagra, Wettingen, Switzerland. Available at nagra.ch.

Schwarz, R., Willmann, M., Reinhardt, S., Hardie, S.M.L., Voss, M., Pechstein, A., 2022b. TBO Bözberg-2-1: Data Report, Dossier VII: Hydraulic Packer Testing. Nagra Arbeitsbericht NAB 21-22, Nagra, Wettingen, Switzerland. Available at nagra.ch.

Schwarz, R., Beauheim, R., Hardie, S.M.L., Pechstein, A., 2022c. TBO Stadel 2-1: Data Report, Dossier VII: Hydraulic Packer Testing. Nagra Arbeitsbericht NAB 22-02, Nagra, Wettingen, Switzerland. Available at nagra.ch.

Schwarz, R., Willmann, M., Fisch, H., Schlickenrieder, L., Voss, M., Pechstein, A., 2022d. TBO Stadel 3-1: Data Report, Dossier VII: Hydraulic Packer Testing. Nagra Arbeitsbericht NAB 22-01, Nagra, Wettingen, Switzerland. Available at nagra.ch.

Schwarz, R., Beauheim, R., Schlickenrieder, L., Manukyan, E., Pechstein, A., 2023. TBO Bachs-1-1: Data Report, Dossier VII: Hydraulic Packer Testing. Nagra Arbeitsbericht NAB 22-04, Nagra, Wettingen, Switzerland. Available at nagra.ch.

SFOE, 2004. Deep geological repositories – Sectoral plan. Swiss Federal Office of Energy SFOE, Bern Switzerland. Available at. www.bfe.admin.ch/bfe/en/home/supply/nuclear-energy/radioactive-waste/deep-geological-repositories-sectoral-plan.html.

Thommes, M., Kaneko, K., Neimark, A.V., Olivier, J.P., Rodriguez-Reinoso, F., Rouquerol, J., Sing, K.S.W., 2015. Physisorption of gases, with special reference to the evaluation of surface area and pore size distribution (IUPAC Technical Report). Pure Appl. Chem. 85, 1051–1069.

Van Laer, L., Aertsens, M., Maes, N., Van Loon, L.R., Glaus, M.A., Wüst, R.A.J., 2023. Diffusion of HTO, ^{36}Cl and ^{22}Na in the Mesozoic rocks of Northern Switzerland: III. Cross-lab comparison of diffusion measurements on argillaceous twin samples. Appl. Geochem., 105840, 2023.105840. https://doi.org/10.1016/j.apgeochem.

Van Loon, L.R., Bunic, P., Frick, S., Glaus, M.A., Wüst, R., 2023. Diffusion of HTO, ^{36}Cl and ^{22}Na in the Mesozoic rocks of Northern Switzerland. I: Effective diffusion coefficients and capacity factors across the heterogeneous sediment sequence. Appl. Geochem., 105843, 2023.105843. https://doi.org/10.1016/j.apgeochem.

Vandenberghe, N., De Craen, M., Wouters, L., 2014. The Boom Clay geology from sedimentation to present-day Occurrence: A review. Memoirs Geol. Surv. Belgium, p. 60.

Wersin, P., Mazurek, M., Mäder, U.K., Gimmi, T., Rufer, D., Lerouge, C., Traber, D., 2016. Constraining porewater chemistry in a 250 m thick argillaceous rock sequence. Chem. Geol. 434, 43–61.

Wersin, P., Traber, D., Mäder, U., Mazurek, M., Waber, H.N., Rufer, D., Gimmi, T., Cloet, V., 2017. Porewater chemistry in claystones in the context of radioactive waste disposal. Procedia Earth Planet. Sci. 17, 718–721.

Wersin, P., Gimmi, T., Mazurek, M., Alt-Epping, M., Pekala, M., 2018. Multicomponent diffusion in a 280 m thick argillaceous rock sequence. Appl. Geochem. 95, 110–123.

Wersin, P., Aschwanden, L., Camesi, L., Gaucher, E., Gimmi, T., Jenni, A., Kiczka, M., Mäder, U., Mazurek, M., Rufer, D., Waber, H.N., Zwahlen, C., Traber, D., 2022. TBO Bözberg-1-1 – Data report, Dossier VIII: Rock properties, porewater characterisation and natural tracer profiles. Nagra Arbeitsbericht NAB 21-21, Nagra, Wettingen, Switzerland. Available at nagra.ch.

Wersin, P., Gimmi, T., Ma, J., Mazurek, M., Zwahlen, E.C., Aschwanden, C., Gaucher, L., Traber, D., 2023. Porewater profiles of Cl and Br in boreholes penetrating the Mesozoic sequence in northern Switzerland. Appl. Geochem., 105845, 2023.105845. https://doi.org/10.1016/j.apgeochem.

Wohlwend, S., Bläsi, H.R., Feist-Burkhardt, S., Hostettler, B., Menkveld-Gfeller, U., Dietze, V., Deplazes, G., 2021a. TBO Bülach-1-1: Data Report, Dossier IV; Microfacies, Bio- and Chemostratigraphic Analysis. Nagra Arbeitsbericht NAB 21-20, Nagra, Wettingen, Switzerland. Available at nagra.ch.

Wohlwend, S., Bläsi, H.R., Feist-Burkhardt, S., Hostettler, B., Menkveld-Gfeller, U., Dietze, V., Deplazes, G., 2021b. TBO Marthalen-1-1: Data Report, Dossier IV; Microfacies, Bio- and Chemostratigraphic Analysis. Nagra Arbeitsbericht NAB 21-20, Nagra, Wettingen, Switzerland. Available at nagra.ch.

Wohlwend, S., Bläsi, H.R., Feist-Burkhardt, S., Hostettler, B., Menkveld-Gfeller, U., Dietze, V., Deplazes, G., 2022. TBO Bözberg-1-1: Data Report, Dossier IV; Microfacies, Bio- and Chemostratigraphic Analysis. Nagra Arbeitsbericht NAB 21-20, Nagra, Wettingen, Switzerland. Available at nagra.ch.

Yu, C., Gonçalves, J., Matray, J.M., 2018. Bayesian inversion of a chloride profile obtained in the hydraulically undisturbed Opalinus Clay: mass transport and paleo-hydrological implications. Appl. Geochem. 93, 178–189.

Zwahlen, C., Aschwanden, L., Camesi, L., Gaucher, E., Gimmi, T., Jenni, A., Kiczka, M., Mäder, U., Mazurek, M., Rufer, D., Waber, H.N., Wersin, P., Traber, D., 2022. TBO Stadel 2-1 – Data report, Dossier VIII: Rock properties, porewater characterisation and natural tracer profiles. Nagra Arbeitsbericht NAB 22-02, Nagra, Wettingen, Switzerland. Available at nagra.ch.

Zwahlen, C., Gimmi, T., Jenni, A., Kiczka, M., Mazurek, M., Van Loon, L.R., Mäder Traber, D., U., 2023. Chloride accessible porosity fractions across the Jurassic sedimentary rocks of northern Switzerland. Appl. Geochem., 105841, 2023.105841. https://doi.org/10.1016/j.apgeochem.